Revision 1

Quantification of dissolved CO_2 in silicate glasses using Micro-Raman spectroscopy.

Yann Morizet[1,2,*], Richard A. Brooker[3], Giada Iacono-Marziano[2] and Bruce A. Kjarsgaard[4]

(1) Laboratoire de Planétologie et Géodynamique de Nantes (LPGN) UMR CNRS 6112, Université de Nantes, Nantes Atlantique Universités, 2 rue de la Houssinière, 44322 NANTES (France)

(2) Institut des Sciences de la Terre D'Orléans (ISTO) UMR CNRS 7327, Université d'Orléans, Campus Géosciences, 1A rue de la Férolerie, 45071 ORLEANS Cedex 2

(3) School of Earth Sciences, University of Bristol, Wills Memorial Building, Queens road, BRISTOL, BS8 1RJ (UK)

(4) Geological Survey of Canada, 601 Booth street, OTTAWA, ON, Canada K1A 0E8

[*]E-mail: yann.morizet@univ-nantes.fr

Abstract

This study investigates the potential use of Confocal Micro-Raman spectroscopy for the quantification of CO_2 in geologically relevant glass compositions. A calibration is developed using a wide range of both natural and synthetic glasses, that have CO_2 dissolved as carbonate (CO_3^{2-}) in the concentration range from 0.2 to 16 wt.%. Spectra were acquired in the 200 and 1350 cm^{-1} frequency region that includes the ν_1 Raman active vibration for carbonate at 1062-1092 cm^{-1} and the intensity of this peak is compared to various other peaks representing the aluminosilicate glass structure. The most precise and accurate calibration is found when carbonate peaks are compared to aluminosilicate spectral features in the high frequency region (HF: 700-1200 cm^{-1}) which can be simulated with several Gaussian peaks, directly related to different structural species in the glass. In some samples the 'dissolved' CO_3^{2-} appears to have two different Raman bands, one sharper than the other. This may be consistent with previous suggestions that CO_3^{2-} has several structural environments in the glass, and is not related to any precipitation of crystalline carbonate from the melt during quenching. The calibration derived using the HF peaks appears linear for both the full range of glass composition considered and the range of CO_2 concentrations, even when multiple carbonate peaks are involved. We propose the following, compositionally independent linear equation to quantify the CO_2 content in glass with micro-Raman spectroscopy:

$$wt.\%\, CO_2 = 15.17 \times {CO_3}/{HF}$$

where CO_3/HF is the area ratio of the fitted ν_1 carbonate peak(s) at 1062-1092 cm^{-1} to the remaining area of the fitted aluminosilicate envelope from 700-1200 cm^{-1}. This is similar to the Raman calibration developed for water, but is complicated by the overlapping of these two fitted components. Using error propagation, we propose the calibration accuracy is better than ±0.4 wt.% CO_2 for our dataset.

42 The ν_1 Raman peak position for carbonate is not constant and appears to be correlated with
43 the density of the melt (or glass) in some way rather than the chemical composition.

44 Keyword: Raman spectroscopy, CO_2 content, silicate glass, melt density, CO_3 molecules
45 Raman shift.

46

47 ## INTRODUCTION

48 Carbon dioxide (CO_2) is generally considered the second most abundant volatile in magmatic
49 systems after water (Gerlach and Graeber 1985; Blank and Brooker 1994; Symmonds et al.
50 1994; Jambon 1994), but can become dominant in some peralkaline igneous provinces, being
51 found at high concentrations in melt inclusions (e.g. Fulignati et al. 2004; . Shimizu et al.
52 2009; Oppenheimer et al. 2011; Mormone et al. 2011; De Moor et al., 2013). Even
53 subordinate concentration of CO_2 can still have a dramatic effect on eruptive processes due to
54 lower saturation levels in decompressing magmas, initiating bubble nucleation and growth
55 (Holloway and Blank 1994; Dixon 1997; Papale and Polacci 1999; Aiuppa et al. 2010).
56 Understanding how magmas transfer and release CO_2 can play an important role in our
57 understanding of the Earth carbon cycle and long term effects on atmospheric fluctuations
58 (Marty and Tolstikhin 1998; Kerrick 2001).

59 There has been considerable experimental effort dedicated to measuring the CO_2 solubility in
60 silicate melts ranging from natural to synthetic systems (e.g. Stolper and Holloway 1988;
61 Fogel and Rutherford 1990; Pan et al. 1991; Dixon and Stolper 1995; Dixon 1997; Jakobsson
62 1997; Tamic et al. 2001; King and Holloway 2002; Behrens et al. 2009; Vetere et al. 2011;
63 Rai et al. 1983; Thibault and Holloway 1994; Brooker et al. 1999, 2001a; Morizet et al. 2002,
64 2010; Botcharnikov et al. 2006). Under oxidizing conditions, CO_2 dissolves in silicate melt as
65 two main species: molecular CO_2 (CO_2^{mol}) and carbonate groups (CO_3^{2-}) (e.g. Fine and
66 Stolper 1985, 1986; Dixon and Stolper 1995; Brooker et al. 1999, 2001b; Morizet et al. 2001,
67 2007). The speciation appears to be related to melt compositions, with CO_2^{mol} dominant in
68 highly silicic, and polymerized quenched glasses (Fine and Stolper 1985; Fogel and
69 Rutherford 1990; Blank et al. 1993; Brooker et al. 1999; Tamic et al. 2001) and CO_3^{2-} groups
70 becoming the dominant species in lower silica or depolymerized compositions such as
71 basaltic glasses (Fine and Stolper 1986; Blank and Brooker 1994; Pan et al. 1991). However,

the extent to which the glass reflects the actual melt speciation is complex (Morizet et al. 2001, 2007; Spickenbom et al. 2010). These experimental studies along with investigation of natural samples have used a wide range of techniques to measure total CO_2 content dissolved in glasses as well as the speciation. These methods range from totally destructive bulk content determinations (manometry, mass spectrometry or LECO^{TM}) to less destructive spectroscopic methods using ion probe (SIMS), infrared (FTIR) or Nuclear Magnetic Resonance (NMR). Each of these methods can have its own advantages and drawbacks related to sample preparation and/or size, or the need for composition dependent calibration.

Micro-Raman spectroscopy is an analytical technique that has rarely been used to examine volatile species in geological glasses (Mysen and Virgo, 1980a, b; Brooker et al. 1999) but is commonly used for studies of fluid inclusions (Dubessy et al. 1989; Morizet et al. 2009). Several attempts have been made to develop a Raman technique to quantify water in glasses (e.g. Thomas 2000; Chabiron et al. 2004; Zajacz et al. 2005; Behrens et al. 2006; Mercier et al. 2009; Le Losq et al. 2012). However, the potential to use Raman as a quantitative tool for CO_2 has not been explored to date. Micro-Raman spectroscopy as an analytical technique has several advantages: 1) it has a very small analytical volume which allows the analysis of <10 µm-size glass inclusions, 2) it is non-destructive and 3) it requires relatively minimal sample preparation. The main drawback has been the assumption that a compositionally dependent calibration would be required.

It has long been known that any Raman vibrational signature of a molecule is proportional to the quantity of the analyzed molecule, but is also a function of the Raman cross-section parameter of the investigated molecular vibration (e.g. Frantz and Mysen, 1995; Burke, 2001; Wu et al., 2004; Mysen, 2007; Morizet et al., 2009). The extent to which the cross section parameter for silicate glass molecular species is dependent on the bulk glass composition is

still matter of debate. However, a compositionally independent calibration has recently been demonstrated for water using the intensity of OH stretching peaks relative to aluminosilicate bands for H_2O contents ranging from 0.2 to above 10 wt.% (Le Losq et al. 2012). This was achieved without needing corrections related to Raman cross-section effects (Mercier et al. 2009; Le Losq et al. 2012). This was surprising given previous attempts to calibrate for water that suggested a significant dependence on the glass compositions (Zajacz et al. 2005; Behrens et al. 2006). One of the objectives of this study is to examine the possibility of developing a similar quantitative technique for CO_2 in glasses that is also independent of composition. In particular, we test the methods considered in previous attempts to calibrate for water, based around the scaling of the H_2O band intensity (I_{H2O}) against the silicate network Raman bands either at high frequency (I_{HF}) or at low frequency (I_{LF}; Mercier et al. 2009). However, the carbonate ν_1 Raman peak used in this study introduces further complication due to the overlap between the carbonate peak(s) position at 1062-1092 cm^{-1} and the silicate network bands in the I_{HF} region from 700-1200 cm^{-1}.

The calibration utilizes a wide range of glass compositions (synthetic and natural) with known CO_2 content ranging from 0.2 wt.% up to 16 wt.%. For this initial investigation we have only considered samples that have all CO_2 dissolved in the form of carbonate species. However, Raman active bands for molecular CO_2 are also easily measured (see Brooker et al. 1999) and could potentially be combined with this technique in the future.

METHODOLOGY

Selected glass samples

The compositions of glasses selected for this study are reported in the Supplementary material. Some features of the natural and synthetic compositions are summarized in Table 1, along with the original reference for the data that has been published. The samples are individual glass chips mounted in epoxy resin blocks (epo-fix) and polished to a finish of 3 μm or better. The data set covers 65 CO_2-bearing samples plus 1 volatile-free sample. The majority of glasses have been previously reported in Brooker et al. (2001a; 2011), Morizet et al. (2002), Iacono-Marziano et al. (2008, 2012) and Brooker and Kjasgaard (2011). A few analyzed samples represent unpublished data from the authors. The investigated glasses cover a wide range of compositions both natural and synthetic. As shown in Table 1, seven samples are natural (trachy-andesite to alkali basalt) from Iacono-Marziano et al. (2008, 2012). Several samples from Brooker et al. (2001a) represent natural compositions (andesite to nephelinite) while others were synthesized in the Na_2O-CaO-Al_2O_3-SiO_2 and Na_2O-CaO-MgO-Al_2O_3-SiO_2 systems. The glasses from Morizet et al. (2002) are haplo-phonolitic in composition. The sample set covers a large compositional range of geological interest: SiO_2 ranges from 30 to 59 wt.%; Al_2O_3 ranges from 4 to 24 wt.%; alkalis range from 0 to 21 wt.% and alkaline-earths range from 2 to 52 wt.% (see Supplementary material for major elements concentrations), although high-silica compositions such as rhyolite are not included as these tend to be dominated by molecular CO_2 species. One useful parameter to distinguish between silica-rich (e.g., rhyolite) and silica-poor (e.g., kimberlite) melts is the degree of depolymerization, usually expressed as NBO/T and defined as the ratio between the concentration of Non-Bridging Oxygen and the concentration of Tetrahedral units (see Mysen 1988; Brooker et al. 2001a). As shown in Table 1, the investigated glasses range from slightly to highly depolymerized compositions, the lowest NBO/T is 0.13 for phonolite RB461, RB465 samples and the highest NBO/T is 2.42 for haplo-kimberlite HK1500 and HK1580 samples. We also indicated the peralkalinity of the glasses defined as the molar

143 (Na_2O+K_2O) / Al_2O_3 ratio and this ranges from 0 to 2.3. The inclusion of iron-free glasses
144 which are colorless and natural iron-bearing glasses that are brown to green in color, allows
145 us to assess the importance of this feature during the analysis (see Le Losq et al., 2012). All
146 the samples were synthesized at high-pressure and high-temperature, the exact synthesis
147 conditions can be obtained from the relevant reference.

148 One important consideration for this initial calibration is that all the dissolved CO_2 in the
149 glass is present as carbonate groups (CO_3^{2-}) with no CO_2^{mol} present. The presence of CO_3^{2-}
150 groups and absence of molecular CO_2 has been established by previous FTIR investigations
151 (Brooker et al. 2001b; Iacono-Marziano et al. 2008, 2012). However, it should be noted that
152 Morizet et al. (2002) suggested that a small fraction (2% relative) of the dissolved CO_2 is
153 present as CO_2^{mol} in haplo-phonolite glasses and a similar small fraction is present in the
154 andesites; this is considered insignificant in the context of our calibration.

155 As reported in Table 1, the glasses cover a CO_2 range from 0.20 to 15.58 wt.%. In the
156 majority of the samples, the CO_2 content was previously determined by LECO bulk analyzer
157 (see Brooker et al. 2001a, 2011; Morizet et al. 2002; Brooker and Kjasgaard 2011). The
158 accuracy and reproducibility for these bulk measurements is on the order of ±0.1 wt.% CO_2.
159 The CO_2 content in the samples from Iacono-Marziano et al. (2008, 2012) was determined by
160 FTIR measurements (with well-established extinction coefficients), with an error believed to
161 be better than ±0.1 wt.%.

162

163 Analytical conditions

164 The Raman scattering was excited using an Innova 300-5W Argon ion laser from Coherent©
165 operating at 514 nm in wavelength and the spectra collected using a Jobin-Yvon Labram

spectrometer (focal distance = 300 mm) equipped with a 2400 grooves/mm grating. The analyses were performed in confocal mode (hole = 500 µm, slit = 200 µm). We performed the analyses using a x50 Olympus objective producing a small analytical volume of a few μm^3. Spectral range covered was between 200 and 1350 cm^{-1}. The spectral frequency position was calibrated using the emission lines of Ne- and Hg-lamps with an accuracy within ±1 cm^{-1}. The output power was set between 50 and 200 mW. We tested the effect of the laser power on the Raman signal for different samples (see Supplementary material for details of analytical conditions). In particular, the sample 2TA2 was analyzed four times at the same sample location but with different laser power from 75 to 200 mW and with an identical acquisition time. The results in terms of CO_2 quantification are almost identical (see Table 2, CO_3/HF ratios) suggesting that this range of laser power does not influence the Raman signal in the studied frequency region. Some samples (Fe-bearing colored glasses for instance) required lower laser power (50 mW) so as to avoid local heating (Behrens et al. 2006; Thomas et al. 2008; Mercier et al. 2009). The absence of local heating of the glass was confirmed by visual inspection with no holes or color change observed. We collected at least two spectra for each sample (except for YP31, with only one spectrum). The acquisition depth was optimized in order to obtain the highest Raman signal (Behrens et al. 2006; Mercier et al. 2009: Le Losq et al. 2012). The acquisition time on a given sample was typically 5 scans for between 20 and 120 sec (10 scans in some cases, see Supplementary material). The spectra were acquired at room temperature and no correction was applied for the dependence of the scattered intensity on temperature and frequency (Neuville and Mysen 1996; Long 2002).

Band assignment

Figure 1 illustrates some typical Raman spectra obtained for different compositions. In Figure 1A, we show several spectra obtained for the YP phonolite composition, while Figure 1B and C show spectra for other selected compositions. The spectra shown in Figure 1A consist of two main characteristic regions: a low-frequency domain (LF) and a high frequency domain (HF). The exact nature of the peaks within and between each frequency domain changes depending on composition. For instance, in YP spectra for phonolite (NBO/T = 0.18) in Figure 1A, the LF is located between 250 and 650 cm^{-1} and the HF between 820 and 1220 cm^{-1} whereas for HK1500 in Figure 1B (highly depolymerized composition, NBO/T = 2.42) the LF is seen between 300 and almost 800 cm^{-1} and the HF starts at 800 and seems to extend to about 1200 cm^{-1}. An increase in depolymerization (increasing NBO/T) produces a shift of the LF towards higher frequency as suggested by previous works (e.g. Mysen et al. 1982; Matson et al. 1983; Wu et al. 2004; Malfait et al. 2007).

The general assignment for the different frequency region has been discussed previously by Mercier et al. (2009). The LF region is a convolution of several individual spectral signatures which are difficult to decipher and as a result the assignment is not straightforward (Rossano and Mysen 2013). In general, this region is considered to represent several vibrational modes: 1) the symmetric stretch of bridging oxygen (BO) within tetrahedral TO_4 units (T = Si, Al; McMillan et al. 1982; Neuville et al. 2004); 2) cation motion in the silicate network (Matson et al. 1983); 3) structural defects in the silicate network (McMillan 1984); 4) three- or four-membered (or higher) ring silicate structural units (Sharma et al. 1981; Galeener 1982; Pasquarello and Car 1998); 5) rocking vibration in polymerized tetrahedral unit (Mysen and Virgo 1980a, b).

The HF region is better understood with peaks assigned to the stretching vibration of various aluminosilicate structural units (Q^n species) that have different numbers of bridging oxygens 'n' such that n is between 0 to 4 (Mysen et al. 1980, 1982; Merzbacher et al. 1991; Mysen

and Richet 2005). A fully polymerized melt structure has all TO_4 units linked with no non-bridging oxygens (NBO/T =0), whilst a fully depolymerized structure has no linked TO_4 tetrahedra and all oxygens are non-bridging such that NBO/T=4. It should be noted that NBO/T and the 'n' value of Q^n species change in the opposite direction with depolymerisation and the 'average' value represent by NBO/T can be made up of differing proportions of various Q^n species. However, this mixture of Q^n units gives an overall shift in the HF envelop to higher frequency as the higher Q^n species become more dominant in more polymerized compositions. The possibility of either Si or charge balanced Al (and possibly other elements) in the T-site introduces further complexity in peak assignment. Comparing spectra in Figure 1 we observe this effect as HK1500 (haplo-kimberlite with NBO/T = 2.42) shows a low frequency HF envelope with a prominent signature centered at 900 cm^{-1} whereas YP spectra (phonolite with NBO/T = 0.18) has a spectral line shape centered at around 1050 cm^{-1}.

Also indicated in Figure 1 is the symmetric stretch (ν_1 CO_3^{2-}) peak for CO_3^{2-} groups which can be observed at positions ranging from 1060 and 1090 cm^{-1} in the glasses of this study. This is within the known range of ν_1 Raman peaks for crystalline carbonates (e.g. Farmer, 1974; Brooker and Bates, 1974; Rutt and Nicola 1974; Cloots 1991; Rividi et al. 2010; Boulard et al. 2012). We observe some variation in ν_1 CO_3^{2-} peak position in different compositions. For example the position of the ν_1 CO_3^{2-} in Figure 1B is 1067 cm^{-1} for BK113 whereas HK1500 is at 1083 cm^{-1}. However there can also be a shift between glasses of the same composition prepared at different conditions.

Background problems

Spectral contamination. In some cases, the true sample signal is difficult to identify due to unwanted background interference. One problem was traced to the Olympus objectives that containing glue which is adding 'contamination' peaks at ~900 and 1300 cm^{-1} (Figure 1C). A similar problem was if epoxy resin of the mount manages to get included in the glass sample. An example is shown in Figure 1C where we show the raw spectrum for RB107 exhibiting both epoxy and the Olympus objective Raman signal contributions. We have corrected for this contamination in the spectra by subtracting 1) the spectrum from the objective taken in air at different acquisition time and 2) the spectrum from the epoxy resin mount (Figure 1C). The resulting spectrum from RB107 after correction in Figure 1C is almost free of spurious signals apart from small sharp peaks at 700 and 925 cm^{-1}; however these features do not affect the fitting for the calibration. A smooth baseline in the 1200-1350 cm^{-1} frequency region is usually a good indicator of a reliable correction as this area should be free of any Raman signal for a silicate glass and therefore totally flat. However, it should be noted that any CO_2 present as the molecular species could give peaks in the 1250 to 1450 region (see Brooker et al. 1999).

Baseline fitting. The high intensity of the Rayleigh scattering line at 0 cm^{-1} produces a slopping background to at least 600 cm^{-1} (Figure 2). As a result, it is necessary to perform a baseline subtraction for uncorrected spectra. The influence of the Rayleigh line at higher frequency (above 800 cm^{-1}) becomes less important. Such baseline subtractions have been discussed extensively (Mercier et al. 2009; Rossano and Mysen 2013; Tarcea and Popp 2013). Mercier et al. (2009) tested two methods: 1) multi-linear baseline fitting (e.g. Robinet et al. 2008) and 2) polynomial spline functions (e.g. Di Muro et al. 2006). Behrens et al. (2006) used the latter method and highlighted the difficulty in defining the parts of the spectrum that are peak-free to be used as reference points for fitting the polynomial function. Although these two methods are the most widely used, other mathematical functions have

263 been considered (Tarcea and Popp 2013). In this study, we followed the method described in
264 Behrens et al. (2006) and Mercier et al. (2009).

265 We fitted a third order polynomial function for the entire spectral range (several examples are
266 included in Figure 2). This baseline fitting procedure used three peak free frequency regions:
267 one between 200 and 300 cm^{-1}, one between 1200 and 1340 cm^{-1} and one intermediate
268 generally located at 800 cm^{-1} (located at 700 cm^{-1} for RB459). The baseline is well simulated
269 using a third-order polynomial equation (indicated next to each curve). Each baseline
270 equation is reported in Supplementary material. In a few cases (RB159 and RB461, see
271 Supplementary material), we were forced to use a fourth-order polynomial equation. Higher
272 order polynomial fits are not desirable as they can produce unwanted oscillation in the
273 baseline (Tarcea and Popp 2013). As seen in Figure 2A and D, some of the baselines fitted in
274 this simplistic way are obviously not a perfect fit to the spectra, especially in the low
275 frequency region below 300 cm^{-1}. However, the baseline fit in the HF reason is generally
276 successful. This may be one reason that our calibration using this region is the most
277 promising and our calibration using LF region produces a much large scatter in the data. As
278 well as the poor baseline fit in the LF region and difficulty in the band assignment, it is also
279 possible that additional vibrational bands for CO_3^{2-} are present in the LF region. These low
280 intensity CO_3^{2-} peaks would always be difficult to identify (making them unsuitable for
281 calibration) but perhaps prominent enough to interfere with the fitting of the main melt
282 structure peaks as required for the calibration. In theory, the ν_4 in-plane bend of a CO_3^{2-}
283 group has a small Raman active band around 680 cm^{-1} and whilst the ν_2 out-of-plane bend at
284 ~880cm-1 is not Raman active, it may become so if certain conditions of local symmetry are
285 imposed.

286

RESULTS: THE CO_2 CALIBRATION METHOD

Spectra simulation based on peak fitting

To develop a robust calibration method we will first identify the spectra features related to the main (volatile-free) melt/glass structure before considering the CO_3^{2-} peak. This is important for the initial step in the spectral simulation procedure. As previously explained, the introduction of more cations (increasing the calculated NBO/T) produces a change in the distribution of the Q^n units that are responsible for the peaks in the HF envelope. A great deal of work has been published on the interpretation of this HF region (e.g. Mysen et al. 1982; Seifert et al. 1982; McMillan 1984; Neuville and Mysen 1996; Rossano and Mysen 2013) and it is important to establish if a full understanding of the peaks involved is important in developing a successful calibration.

Our fitting procedure involves fitting several Gaussian peaks to simulate the entire HF envelope. The assignment of each individual Gaussian peak can be made after the simulation is completed, and although we show that this assignment is not essential for our calibration, it is important that the results broadly conform to our general understanding peak distributions as a function of composition. A recent review by Rossano and Mysen (2013) shows typical examples of the simulations of the Raman spectra. Invariably, recurrent positions are obtained for the individual Gaussian peaks approximately centered near ~1150, ~1070, ~1020, ~950 cm^{-1}. These positions varying as a function of composition (Malfait et al. 2007; 2008) as do the relative heights. Additional Raman features have also been observed at lower frequency. Early works (Brawer and White 1977; Furukawa et al. 1981; Mysen et al. 1982) suggest that another Gaussian centered at 860 cm^{-1} may be assigned to Q^0 species whereas Q^1 species may be represented by a peak at 900 cm^{-1} (McMillan 1984). For our purpose, the

detailed assignment of each individual Gaussian proves to be unimportant as we show that the calibration is dependent only on the area beneath the entire HF region.

For the calibration, the spectral fitting of the aluminosilicate structural units (Q^n) and the ν_1 CO_3^{2-} signature were simulated together. The simulations were conducted with Origin 7.5© software fitting package. The selection of initial input parameters are important for an accurate simulation but as previously stated these are dependent on the glass composition. We show typical simulations obtained for several samples in Figure 3 and 4. The whole set of fitted parameters include peak positions, full width at half maximum (FWHM) and areas with associated error are all reported in Supplementary material, but in Table 2 there is a summary of the peak position for the ν_1 CO_3^{2-} peak and Q-species peaks. It should be emphasized that each proposed simulations is not unique and represents one of several possible fits.

The fitting procedure for the calibration is described below, but for the YP haplo-phonolite samples we also have the Raman spectrum of the volatile-free sample (YPF) allowing a more rigorous testing of the fitting for the CO_2-free part of the structure. We simulated the CO_2-free YPF haplo-phonolite spectra with four individual Gaussian peaks (Figure 3A) corresponding to various aluminosilicate Q^n structural units. Two spectra were simulated at the same time so as to provide better constraints on the iterative procedure and the simulation was conducted as follow:

- The four peaks were located at 920, 1000, 1050 and 1120 cm^{-1}, based on previous investigations (e.g. Rossano and Mysen 2013).
- The FWHM of each peak was fixed at 65 cm^{-1}.
- A first set of iterations was performed to adjust the area of each Gaussian peak to give the best fit possible at this stage. The position and the FWHM are fixed during this step. The resulting quality of fit (expressed as χ^2) is usually high.

- During the second iterative step, the areas and peak position are left free to evolve. The iteration is performed until the χ^2 does not change.
- With the peak position fixed from the second step. A third step is performed where the FWHM and peak areas are optimized until the χ^2 does not change.
- The second and third steps are repeated several times until we obtain the best fit (lowest χ^2) possible.

As seen in Figure 3A, the resulting simulation reproduces the actual Raman spectrum well as shown by the plot of residual data. For this haplo-phonolite we obtained the following positions for the individual Gaussian: 921.2, 997.7, 1070.2 and 1132.6 cm^{-1}. The FWHM obtained are 78.6, 85.9, 96.5 and 95.6, respectively. The error on the peak position and FWHM is less than 1 cm^{-1}.

The simulation of the YP CO_2-bearing haplo-phonolite spectra was conducted in a similar way to the YPF CO_2-free sample; however, we added an additional band corresponding to the CO_3^{2-} vibrational peak. The peak positions and the FHWM obtained for YPF were transferred to the CO_2-bearing YP samples. This procedure is justified by constant composition but does make the assumption that the dissolved carbonate is not affecting the Q^n species distribution significantly. For these simulations, the peak position and the FWHM of the Q-species structural units are fixed and one extra peak added to simulate the ν_1 for CO_3^{2-}. This peak alone is then left totally free to evolve. As shown in Figure 3, the simulation of the ν_1 CO_3^{2-} peak gives similar results (peak position and FWHM) in all the YP CO_2-bearing samples. The low residual demonstrate the reliability of our simulation. As expected, the ν_1 CO_3^{2-} shows an increasing intensity with increasing CO_2 content. The ν_1 CO_3^{2-} peak position is approximately 1082 cm^{-1}. The ν_1 CO_3^{2-} FWHM exhibits more variability with a range between 34 and 46 cm^{-1} (see Table 2). The increase in FWHM seems to be correlated to the total CO_2 content:

358 the lowest FWHM (34 cm^{-1}) is obtained for YP34 with 0.66 wt.% CO_2 whereas the highest
359 FWHM (46 cm^{-1}) is obtained for YP4 with 1.99 wt.% CO_2 (Table 2).

360 The FWHM for the fitted ν_1 CO_3^{2-} peak has a value which is well-below the FWHM values
361 of the Q-species structural units (> 78 cm^{-1}). This observation is important because we can,
362 subsequently constrain the robustness of our simulation by considering that ν_1 CO_3^{2-} will
363 have an FWHM not exceeding a certain value.

364 For other samples, a volatile-free equivalent glass was not available, so the Raman spectrum
365 simulation was more complicated. Ideally the initial guess for the Gaussian peak parameters
366 should be totally free, but we introduced the assumption that Q^n Gaussian peaks must be
367 wider than the ν_1 CO_3^{2-}: on the order of 60-70 cm^{-1} for Q^n and less than 30-40 cm^{-1} for ν_1
368 CO_3^{2-}. A second assumption is that the individual Q^n Gaussian peak position are known
369 approximately and are a strong function of the initial chemical composition (e.g. Malfait et al.
370 2007; Rossano and Mysen 2013). A glass with a high NBO/T will have HF region shifted to a
371 lower frequency whereas a low NBO/T glass has the HF region shifted to the higher
372 frequency (see Figure 1 and 2). The distribution of area between Gaussian peaks for different
373 Q^n species also changes with NBO/T in a way generally consistent with current
374 understanding.

375 We show several simulation results in Figure 4 and there is clearly an increase in the intensity
376 of the fitted ν_1 CO_3^{2-} peak with concentration. For example, the simulation for BK115 (Figure
377 4C) with 11.47 wt.% CO_2 shows a considerably more intense ν_1 CO_3^{2-} peak compared with
378 the simulation for 2TA1 (Figure 4A) with 0.32 wt.% CO_2. The ν_1 CO_3^{2-} peak position shows
379 more variability compared to YP samples as might be expected for the range of compositions
380 with peak position ranging from 1062 to 1092 cm^{-1}. The FWHM of the ν_1 CO_3^{2-} peak is on
381 the same order as for YP samples with values ranging from 5 to 45 cm^{-1} (Table 2). The

narrowest peaks are observed for very specific samples that in fact require two fitted peaks for CO_3^{2-}. An obvious example is shown for RB66 (Figure 4F) and suggests there are at least two CO_3^{2-} environments present in these glasses. This is consistent with the fact that certain glasses in this study (from Brooker and Kjarsgaard 2011) have been synthesized as the silicate component of a silicate-carbonate immiscible pair or synthesized in the one liquid regions, but close to the two liquid solvus and in both cases these melts could enter the two liquid region during quenching. Most samples in this study are very clear, but a few have been included that range from 'opalescent' to 'milky'. We have considered that some carbonate liquid may have been exsolved on a microscopic scale during quenching, subsequently crystallizing to give a second sharper ν_1 CO_3^{2-} peak as expected for crystalline carbonates. However, there is no correlation between the presence of the second peak and the clarity or 'milkyness' of the sample. All the samples with two peaks are optically clear apart from RB66 and RB163, whereas several opalescent samples have only one peak (BK 32, 39, 48 and RB8).

Although, it adds another variable in the simulation of the spectra, the residual plot shows that the spectra can be simulated with good accuracy where two carbonate peaks are required. Even when the samples are opalescent and/or have two peaks such as RB66, the peaks areas still seem to give the correct quantification in the following calibration.

A linear calibration for total CO_2 content

Following previous studies (Thomas 2000; Zajacz et al. 2005; Behrens et al. 2006; Mercier et al. 2009) that investigated the relationship between the areas of the broad water band at 3550 cm^{-1} and the silicate glass structure (either the HF or LF) we have applied the same procedure to see if the ratio of the ν_1 CO_3^{2-} to HF peak areas is proportional to the total CO_2 content.

406 The LF areas were also considered but produce poor results for the reasons previously
407 described; in particular the difficulty of fitting a third-order polynomial baseline underneath
408 the LF region.

409 The CO_3/HF results are shown in Table 2. Several spectra were taken for each glass to test for
410 homogeneity and reproducibility, which are discussed along with other sources of error
411 below. In Figure 5 the entire set of CO_3/HF ratios are plotted against the wt.% CO_2 as
412 measured by bulk analyses or FTIR. Figure 5B has a more detailed view of the dataset at low
413 CO_2 content below 1 wt.% CO_2 but above our estimated minimum detection limit of 0.2
414 wt.%. The dataset is presented in three groups: 1) the YP haplo-phonolite samples (constant
415 composition), 2) the other compositions for which the simulation lead to one single ν_1 CO_3^{2-}
416 peak and 3) the compositions for which two ν_1 CO_3^{2-} peaks were needed for the simulation.
417 Perhaps surprisingly, we observe that this third group does not noticeably depart from the
418 linear trend established by the other two groups.

419 In Figure 5B the shaded area illustrates our minimum detection limit (m.d.l.) where it was not
420 possible to resolve CO_3^{2-} peaks from the silicate envelope. Our attempt to simulate the
421 spectra for an alkali-basalt with a CO_2 content lower than 0.2 wt.% did not require any peak
422 at ~1070 cm^{-1} making it impossible to obtain a CO_3/HF ratio.

423 The excellent linear correlation of the ν_1 CO_3^{2-} intensity as a function of total CO_2 content
424 (Figure 5), allows us to propose the following linear equation for the entire 143 point dataset:

425 $$wt.\%\, CO_2 = 15.17 \times {CO_3}/{HF} \qquad \text{Eq. 1}$$

426 This equation leads to a correlation factor of 0.9747. Included in Table 2 is the calculated
427 CO_2 content from this linear regression and the corresponding CO_3/HF with its associated
428 error. This can be compared with the actual measured value as presented in Table 1.

429

430 Sources of error in the Raman measurements and linear fit

431 We have considered several sources of error associated with either the samples themselves or
432 the simulation of the Raman spectra or the linear fit. The error associated with any sample
433 heterogeneity can be represented by the standard deviation (1σ) obtained on replicated
434 CO_3/HF ratios. For a few samples, we did observe a significant range of CO_3/HF values. For
435 instance if we consider the CO_3/HF given in Table 2 for HK1500 and calculate the average
436 and standard deviation of the CO_3/HF ratio we obtain a value of 0.540±0.064 (see
437 Supplementary material). This standard deviation value corresponds to a CO_2 change on the
438 order of ±1.0 wt.% or 12% relative. The CO_3/HF standard deviation calculated for all
439 samples excluding HK1500 is far less than this, averaging ±0.010 which corresponds to
440 ±0.15 wt.% CO_2. This suggests that we can consider that the investigated glass samples are
441 homogeneous and the spectra features are highly reproducible.

442 The second type of error is related to the simulation itself. The error reported by the fitting
443 software probably underestimates the true error on the calculated CO_3/HF ratio. We have
444 tested several ways to provide a more realistic error on each CO_3/HF value. The first attempt
445 was to change the position of the ν_1 CO_3^{2-} peak and quantify the corresponding change in the
446 peak area. For each Raman spectrum, we have one data point every 1 cm^{-1}; therefore we have
447 applied a variation of ±0.5 cm^{-1} in the ν_1 CO_3^{2-} peak position which is more than twice the
448 software reported error (±0.2 cm^{-1}). Adopting this procedure did not produce any significant
449 error on the CO_3/HF ratio. Even for the samples with the lowest CO_2 content (e.g. #4-3), the
450 calculated error of less than 0.05 wt.% CO_2 is not significant.

451 The third source of error is related to the estimated peaks areas. Following Mysen et al.
452 (1982) we have applied 5% error on the fitted peak areas and this was propagated through
453 standard error calculation to the CO_3/HF ratios. The resulting error is given in Table 2 for
454 each CO_3/HF value. The largest error (1σ) on the CO_3/HF is generated for the RB8 analyses
455 giving ±0.080 on the CO_3/HF (see Table 2). In term of CO_2 content, this corresponds to ±1.25
456 wt.% CO_2 (or 8% relative). The lowest error on the CO_3/HF is on the order of ±0.001 (see
457 Table 2) which corresponds to about 5% relative for RB466 (1.1 wt%) and #4-4 (0.43 wt%).
458 The average of all the calculated the peak area errors (see Supplementary material) is ±0.018
459 on the CO_3/HF, which corresponds to ±0.3 wt.% CO_2.

460 A fourth source of error related to the linear regression in Figure 5. As shown for Eq. 1, the
461 scaling factor relating the CO_2 content to the CO_3/HF is 15.17 with an error of ±0.17. This
462 value represents the error in 1σ for 95% confidence interval. The linear fit also gives the
463 lower and upper limit confidence intervals which are 14.83 and 15.51, respectively. These
464 two values lead to an error on the 95% confidence interval of ±0.34. This error value is of a
465 similar order to the 5% error applied to the peaks area.

466 Considering the different types of error mentioned above, the expected accuracy for the
467 calibrated CO_2 content determination is much better than ±0.4 wt.% CO_2. This is not as
468 precise or as sensitive as some other techniques such as IR at low concentrations of CO_2, but
469 is comparable at higher concentrations and could be considered more accurate as it is
470 independent of compositional factors such as IR extinction coefficients.

471 There is one further potential source of error related to the Raman scattering cross-sections
472 for the different Q^n species and indeed the carbonate. In common with the water calibration
473 of Le Losq et al. (2012) we observe a direct and linear relationship between CO_3/HF ratios
474 and the volatile content. This implies that the average Raman scattering cross section of all

475 the different Q^n species in the HF envelope is always the same and additionally that the
476 carbonate scattering cross-section (and OH) is also independent of composition. However,
477 current knowledge of the Raman scattering cross-sections for the different Q^n species,
478 suggest they vary considerably (see Frantz and Mysen 1995). The molecular dynamic
479 simulations of Wu et al. (2004) suggest the peak area for the same mol.% of silicate
480 tetrahedral may fall by half as the Q^n distribution changes between NBO/T values of 2 and 1
481 and by half again between 1 and 0. For a constant area carbonate peak this should introduce a
482 compositional dependence that will double the apparent amount of carbonate each time. Our
483 calibration clearly demonstrated that this is not the case and the fixed carbonate area
484 represents the same amount of CO_2. Le Losq et al. (2012) suggests that the Raman cross-
485 section coefficients are cancelled by the baseline subtraction therefore allowing the direct use
486 of species ratio (i.e. water / silicate glass) for quantitative purposes. An alternative is that the
487 carbonate (and OH) peak cross section changes with composition in a way that exactly
488 cancels out the Q-species compositional effect. Without a systematic study involving specific
489 compositions designed to test these theories, we can only claim our empirical observation
490 appears to work in the same way as the water calibration of Le Losq et al. (2012) and it is not
491 possible to evaluate any associated error.

492

493 Spectral characteristics of the carbonate group in glasses

494 The shifting position of the fitted carbonate peak has been noted above and can be seen in
495 Table 2. Although these fitted ν_1 peak positions are in the general range for crystalline
496 carbonates, they do not match the exact position for the corresponding cations between
497 crystals and even the more simple glass compositions where the cation options are limited.
498 Attempts to correlate this shift against various compositional parameters (cation

499 concentrations, NBO/T and peralkalinity) also proved unsuccessful. However, the samples
500 made at higher pressures did tend the have peaks at higher frequencies and some correlation
501 was found between the peak position and the estimate melt density (at run conditions). This is
502 actually difficult to quantify in a meaningful way as the melt has a different density to the
503 glass, which has its structure 'frozen in' at the pressure-temperature conditions of the glass
504 transition (Tg). This depends on the P-T path during quenching of the experiment and Tg has
505 a compositional dependence that is also difficult to estimate accurately. In addition, the CO_2
506 speciation may have a different 'effective Tg' to the traditional melt structure value and some
507 unobserved molecular CO_2 may also be being converted to carbonate during quenching
508 (Morizet et al. 2007; Spickenbom et al. 2010). In Figure 6 we use the dataset for haplo-
509 phonolite to make the empirical observation that for a single composition (i.e. with a
510 relatively constant Tg value) the peak shifts to higher frequency with calculated melt density
511 using Lange and Carmichael (1990) model, pressure having the most obvious effect. Similar
512 effects can be seen for the andesite (RB466 & 459) and Fe-Phonolite (RB 465 & 461) at 1.5
513 to 2.0 GPa as well as the more depolymerised composition (NBO/T = 2) of R85Ca10 and
514 R85Ca15 from 1.0 to 1.5 GPa. This suggests the ν_1 C-O stretching mode of the carbonate
515 maybe partly constrained by the physical constriction of the surrounding aluminosilicate
516 network rather than being controlled by solely by variations in the local coordinating cations
517 that are responsible for the position shift in crystalline materials (Farmer, 1974; Brooker and
518 Bates, 1974).

519

520 ## APPLICATION OF THE TECHNIQUE

521 This study has established both the potential and limitations for the use of Micro-Raman
522 spectroscopy in the quantitative analysis of CO_2 in aluminosilicate glasses. The method used

523 to calibrate the CO_2 content via Raman spectroscopy is similar to the most recent calibration
524 developed for H_2O content in glasses, using the area ratio of a volatile species peak to
525 aluminosilicate peaks between 800 and 1200 cm^{-1}. For CO_2 (in this case represented by
526 dissolved carbonate species) there is the added complication that the Raman active ν_1 peak(s)
527 for CO_3^{2-} are between 1060 and 1090 cm^{-1} and therefore overlap with this aluminosilicate
528 region. Ultimately, it is this overlap that limits the sensitivity of the technique to CO_2 content
529 above 0.2 wt.%, but it appears possible to accurately identify the carbonate component of the
530 HF envelope at higher concentrations up to at least 16 wt.%. Unfortunately, the lower
531 detection level will limit the application of Raman for the majority of natural volcanic
532 systems where concentrations tend to be lower. However, the technique has great potential
533 for some peralkaline volcanoes, especially where silicate melts are associated with
534 carbonatites (Mitchell and Dawson 2012; Guzmics et al. 2012; De Moor et al. 2013). In
535 addition, silicate glass is constantly being discovered in mantle xenoliths where it is
536 sometime associated with carbonates (Amundsen 1989; Pyle and Haggerty 1994; Kogarko et
537 al. 2001; Laurora et al. 2001; Hurai et al. 2007). The issue of what these mantle carbonates
538 represent (solid phases or quenched immiscible melts) may be evaluated by analysis of the
539 CO_2 content of the silicate glass.

540 However, the most useful application for this technique will be the analysis of silicate melts
541 in high pressure, experimental studies. Especially those investigating carbonate-silicate melt
542 immiscibility (e.g., Brooker and Kjarsgaard 2011) and carbonated mantle melting (e.g.,
543 Dalton and Presnall 1998; Moore and Wood 1998; Dasgupta et al. 2006). With increasing
544 pressure the experimental samples become ever smaller and difficult to analyze with other
545 techniques, particularly when small pockets of partial melt are involved. In theory, the
546 simultaneous analysis of both water and CO_2 in glasses should be possible with this

technique, although this remains to be tested. The possibility of measuring molecular CO_2 is also an area that may be developed in the future.

The linear nature of the calibration also has interesting implications for Raman investigations of silicate glass structure and the CO_2 solubility mechanism. As previously discussed, the most striking feature of Figure 5 is the clear linear correlation between the CO_3/HF ratio and the measured CO_2 content over the whole range of compositions considered. Whilst clearly a desirable result, this independence from the glass composition is perhaps an area requiring further investigation as it remains at odds with our understanding of the Raman scattering coefficients (see above). One possibility is that different Q^n species in HF region could be related to specific NBOs that favor a reaction with CO_2 to give CO_3^{2-} (Brooker et al. 2001a; Iacono-Marziano et al. 2012) and this counteracts the scattering cross sectional effect in a systematic way.

Another important aspect related to silicate melt structure is the way the peak position for the CO_3^{2-} ν_1 vibration mode appears to shift with calculated melt density. This is different to the shift observed in crystalline carbonates resulting from the substitution of cations with different radii, although these solid materials do also demonstrate a peak shift related to pressure. The glass shift may represent a response of this symmetric vibration to the 'physical' confining nature of the surrounding melt structure. This is in contrast to the ν_3 asymmetric CO_3^{2-} mode investigated by infrared spectroscopy, which appears to be more sensitive to the 'chemical' nature or surrounding cations (Brooker et al., 2001b). Whether the shift in silicate glasses has potential to estimate the quenching pressure for melt inclusions remain to be explored.

Acknowledgement

The authors are grateful to the University of Orléans, the University of Nantes, the University of Bristol and the CNRS for their financial support and access to analytical facilities. We would like to thank B.O. Mysen for handling the manuscript and the constructive reviews by two anonymous reviewers which greatly improved the quality of the manuscript.

References

Aiuppa, A., Bertagnini, A., Metrich, N., Moretti, R., Di Muro, A., Liuzzo, M., and Tamburello, G. (2010) A model of degassing for Stromboli volcano. Earth Planetary Science Letters, 295, 195-204.

Amundsen, H.E.F. (1987) Evidence for liquid immiscibility in the upper mantle. Nature, 327, 692-695.

Behrens, H., Roux, J., Neuville, D.R., and Siemann, M. (2006) Quantification of dissolved H_2O in silicate glasses using confocal microRaman spectroscopy. Chemical Geology, 229, 96–112.

Behrens, H., Misiti, V., Freda, C., Vetere, F., Botcharnikov, R.E., and Scarlato, P. (2009) Solubility of H_2O and CO_2 in ultrapotassic melts at 1200 and 1250°C and pressure from 50 to 500 MPa. American Mineralogist, 94, 105–120.

592 Blank, J.G., Stolper, E.M., and Carroll, M.R. (1993) Solubilities of carbon dioxide and water
593 in rhyolitic melt at 850°C and 750 bars. Earth Planetary Science Letters, 119, 27-36.

594

595 Blank, J.G. and Brooker, R.A. (1994) Experimental studies of carbon dioxide in silicate
596 melts: solubility, speciation and stable isotope behavior. In: Carroll M.R., Holloway J.R. (eds)
597 Volatiles in magmas. (Reviews in mineralogy) Mineralogical Society of America, Washington, DC
598 30, 157–186.

599

600 Botcharnikov, R.E., Behrens, H., and Holtz, F. (2006) Solubility and speciation of C–O–H
601 fluids in andesitic melt at T=1100–1300°C and P=200 and 500 MPa. Chemical Geology, 229,
602 125–143.

603

604 Boulard, E., Guyot, F., and Fiquet, G. (2012) The influence on Fe content on Raman spectra
605 and unit cell parameters of magnesite-siderite solid solutions. Physics and Chemistry of
606 Minerals, 39, 239-246.

607

608 Brawer, S.A. and White, W.B. (1977) Raman spectroscopic investigation of the structure of
609 silicate glasses. II. Soda-alkaline earth-alumina ternary and quaternary glasses. Journal of
610 Non-Crystalline Solids, 23, 261-278.

611

612 Brooker, M.H. and Bates, J.B. (1974) Raman and infrared spectral studies of anhydrous
613 potassium and rubidium carbonates. Spectrochimica Acta, 80, 2211-2220.

Brooker, R.A., Kohn, S.C., Holloway, J.R., McMillan, P.F., and Carroll, M.R. (1999) Solubility, speciation and dissolution mechanisms for CO_2 in melts on the $NaAlO_2$-SiO_2 join. Geochimica Cosmochimica Acta, 63, 3549-3565.

Brooker, R.A., Kohn, S.C., Holloway, J.R., and McMillan, P.F. (2001a) Structural controls on the solubility of CO_2 in silicate melts. Part I: Bulk solubility data. Chemical Geology, 174, 225–240

Brooker, R.A., Kohn, S.C., Holloway, J.R., and McMillan, P.F. (2001b) Structural controls on the solubility of CO_2 in silicate melts. Part II: IR characteristics of carbonate groups in silicate glasses. Chemical Geology, 174, 241–254.

Brooker, R.A., Sparks, R.S.J., Kavanagh, J.L., and Field, M. (2011) The volatile content of hypabyssal kimberlite magmas: some constraints from experiments on natural rock compositions. Bulletin of Volcanology, 73, 959-981.

Brooker, R.A. and Kjasgaard, B.A. (2011) Silicate-carbonate liquid immiscibility and phase relations in the System SiO_2-Na_2O-Al_2O_3-CaO-CO_2 at 0.1-2.5 GPa with applications to carbonatite genesis. Journal of Petrology, 52, 1281-1305.

635

636 Burke, E.A.J. (2001) Raman microspectrometry of fluid inclusions. Lithos 55, 139–158.

637

638 Chabiron, A., Pironon, J., and Massare, D. (2004) Characterization of water in synthetic
639 rhyolitic glasses and natural melt inclusions by Raman spectroscopy. Contribution to
640 Mineralogy and Petrology, 146, 485-492.

641

642 Cloots, R. (1991) Raman spectrum of carbonates $MnCO_3$ in the 1100-1000 cm^{-1} region:
643 observation of the ν_1 mode of the isotopic $(C^{16}O_2{}^{18}O)^{2-}$ ion. Spectrochimica Acta A, 47,
644 1745-1750.

645

646 Dalton, J.A. and Presnall, D.C. (1998) The continuum of primary carbonatitic–kimberlitic
647 melt compositions in equilibrium with lherzolite: data from the system $CaO–MgO–Al_2O_3–$
648 $SiO_2–CO_2$ at 6 GPa. Journal of Petrology, 39, 1953–1964

649

650 Dasgupta, R., Hirschmann, M.M., and Stalker, K. (2006) Immiscible transition from
651 carbonate-rich to silicate-rich melts in the 3 GPa melting interval of eclogite + CO_2 and
652 genesis of silica-undersaturated Ocean Island Lavas. Journal of Petrology, 47, 647-671.

653

654 De Moor, J.M., Fischer, T.P., King, P.L., Botcharnikov, R.E., Hervig, R.L., Hilton, D.R.,
655 Barry, P.H., Mangasini, F., and Ramirez, C. (2013) Volatile-rich silicate melts from Oldoinyo

Lengai volcano (Tanzania): Implications for carbonatite genesis and eruptive behavior. Earth and Planetary Science Letters, 361, 379-390.

Di Muro, A., Villemant, B., Montagnac, G., Scaillet, B., and Reynard, B. (2006) Quantification of water content and speciation in natural silicic glasses (phonolite, dacite, rhyolite) by confocal microRaman spectrometry. Geochimica Cosmochimica Acta, 70, 2868-2884.

Dixon, J.E. and Stolper, E.M. (1995) An experimental study of water and carbon dioxide solubilities in mid-ocean ridge basaltic liquids. Part II: Application to Degassing. Journal of Petrology, 36, 1633– 1646.

Dixon, J.E. (1997) Degassing of alkalic basalts. American Mineralogist, 82, 368–378.

Dubessy, J., Poty, B., and Ramboz, C. (1989) Advances in C–O–H–N–S fluid geochemistry based on micro-Raman spectrometric analysis of fluid inclusions. European Journal of Mineralogy, 1, 517–534.

Farmer, V.C. (1974) The Infrared Spectra of Minerals. Mineralogical Society, London, 539 pp.

677 Fine, G. and Stolper, E.M. (1985) The speciation of carbon dioxide in sodium aluminosilicate
678 glasses. Contribution to Mineralogy and Petrology, 91, 105–121.

679

680 Fine, G. and Stolper, E.M. (1986) Dissolved carbon dioxide in basaltic glasses:
681 concentrations and speciation. Earth Planetary Science Letters, 76, 263–278.

682

683 Fogel, R.A. and Rutherford, M.J. (1990) The solubility of carbon dioxide in rhyolitic melts:
684 A quantitative FTIR study. American Mineralogist, 75, 1311–1326.

685

686 Frantz, J.D. and Mysen, B.O. (1995) Raman spectra and structure of $BaO\text{-}SiO_2$, $SrO\text{-}SiO_2$,
687 and $CaO\text{-}SiO_2$ melts to 1600°C. Chemical Geology, 121, 155-176.

688

689 Fulignati, P., Marianelli, P., Métrich, N., Santacroce, R., and Sbrana, A. (2004) Towards a
690 reconstruction of the magmatic feeding system of the 1944 eruption of Mt Vesuvius. Journal
691 of Volcanology and Geothermal Research, 133,13-22.

692

693 Furukawa, T., Fox, K.E., and White, W.B. (1981) Raman spectroscopic investigation of the
694 structure of silicate glasses. III. Raman intensities and structural units in sodium silicate
695 glasses. Journal of Chemical Physics, 75, 3226–3237.

696

697 Galeener, F.L. (1982) Planar rings in glasses. Solid State Communications, 44, 1037–1040.

Gerlach, T.M. and Graeber, E.J. (1985) Volatile budget of Kilauea volcano. Nature, 313, 273-277.

Guzmics T., Mitchell, R.H., Szabo, C., Berkesi, M., Milke, R., and Ratter, K. (2012) Liquid immiscibility between silicate, carbonate and sulfide melts in melt inclusions hosted in co-precipitated minerals from Kerimasi volcano (Tanzania): evolution of carbonated nephelinitic magma. Contributions to Mineralogy and Petrology, 164, 101–122

Holloway, J.R. and Blank, J.G. (1994) Application of experimental results to C-O-H species in natural melts. In: Carroll M.R., Holloway J.R. (eds) Volatiles in magmas. (Reviews in mineralogy) Mineralogical Society of America, Washington, DC 30, pp 157-230.

Hurai, V., Huraiova, M., Konecny, P., and Thomas, R. (2007) Mineral-melt-fluid composition of carbonate-bearing cumulate xenoliths in Tertiary alkali basalts of southern Slovakia. Mineralogical Magazine, 71, 63-79.

Iacono-Marziano, G., Gaillard, F., and Pichavant, M. (2008) Limestone assimilation by basaltic magmas: an experimental re-assessment and application to Italian volcanoes. Contribution to Mineralogy and Petrology, 155, 719-738.

719 Iacono-Marziano, G., Morizet, Y., Le Trong, E., and Gaillard, F. (2012) New experimental
720 data and semi-empirical parameterization of H_2O-CO_2 solubility in mafic melts. Geochimica
721 Cosmochimica Acta, 97, 1-23.

722

723 Jakobsson, S. (1997) Solubility of water and carbon dioxide in an icelandite at 1400°C and 10
724 kilobars. Contribution to Mineralogy and Petrology, 127, 129-135.

725

726 Jambon, A. (1994) Earth degassing and large-scale geochemical cycling of volatile elements.
727 In: Carroll M.R., Holloway J.R. (eds) Volatiles in magmas. (Reviews in mineralogy)
728 Mineralogical Society of America, Washington, DC, 30, pp 479-517.

729

730 Kerrick, D.M. (2001) Present and past nonanthropogenic CO_2 degassing from the solid Earth.
731 Reviews of Geophysics, 39, 565-585.

732

733 King, P.L. and Holloway, J.R. (2002) CO_2 solubility and speciation in intermediate
734 (andesitic) melts: the role of H_2O and composition. Geochimica Cosmochimica Acta, 66,
735 1627–1640.

736

737 Kogarko, L.N., Kurat, G., and Ntaflos, T. (2001). Carbonate metasomatism of the oceanic
738 mantle beneath Fernando de Noronha Island, Brazil. Contributions to Mineralogy and
739 Petrology, 140, 577-587.

Lange, R., and Carmichael, I.S.E (1990) Thermodynamic properties of silicate liquids with emphasis on density, thermal expansion and compressibility. In: Nicholls J. and Russell J.K. (eds) Modern methods of igneous petrology: Understanding magmatic processes (Reviews in Mineralogy) Mineralogical Society of America, Washington, DC, 24, pp 25-64.

Laurora, A., Mazzucchelli, M., Rivalenti, G., Vannucci, R., Zanetti, A., Barbieri, M.A., and Cingolani, C.A. (2001). Metasomatism and melting in carbonated peridotite xenoliths from the mantle wedge: The Gobernador Gregores case (southern Patagonia). Journal of Petrology, 42, 69-87.

Le Losq, C., Neuville, D.R., Moretti, R., and Roux, J. (2012) Determination of water content in silicate glasses using Raman spectrometry: Implications for the study of explosive volcanism. American Mineralogist, 97, 779-790.

Long, D.A. (2002). The Raman Effect: A Unified Treatment of the Theory of Raman Scattering by Molecules. John Wiley and Sons, Eds pp. 598.

Malfait, W.J., Zakaznova-Herzog, V.P., and Halter, W.E. (2007) Quantitative Raman spectroscopy: High-temperature speciation of potassium silicate melts. Journal of Non-Crystalline Solids, 353, 4029-4042.

762 Malfait, W.J., Zakaznova-Herzog, V.P., and Halter, W.E. (2008) Quantitative Raman
763 spectroscopy: Speciation of Na-silicate glasses and melts. American Mineralogist, 93, 1505-
764 1518.

765

766 Marty, B. and Tolstikhin, I.N. (1998) CO_2 fluxes from mid-ocean ridges, arcs and plumes.
767 Chemical Geology, 145, 233-248.

768

769 Matson, D.W., Sharma, S.K., and Philpotts, J.A. (1983) The structure of high-silica alkali-
770 silicate glasses. A Raman spectroscopic investigation. Journal of Non-Crystalline Solids, 58,
771 323-352.

772

773 McMillan, P.F., Piriou, B., and Navrotsky, A. (1982) A Raman spectroscopic study of glasses
774 along the joins silica-calcium aluminate, silica-sodium aluminate, and silica-potassium
775 aluminate. Geochimica Cosmochimica Acta, 46, 2021-2037.

776

777 McMillan, P.F. (1984) Structural studies of silicate glasses and melts - applications and
778 limitations of Raman spectroscopy. American Mineralogist, 69, 622-644.

779

780 Mercier, M., Di Muro, A., Giordano, D., Métrich, N., Lesne, P., Pichavant, M., Scaillet, B.,
781 and Clocchiatti, R. (2009) Influence of glass polymerisation and oxidation on micro-Raman
782 water analysis in alumino-silicate glasses. Geochimica Cosmochimica Acta, 73, 197–217.

Merzbacher, C.I. and White, W.B. (1991) The structure of alkaline earth aluminosilicate glasses as determined by vibrational spectroscopy. Journal of Non-Crystalline Solids, 130, 18-34.

Mitchell, R.H. and Dawson, J.B. (2012) Carbonate–silicate immiscibility and extremely peralkaline silicate glasses from Nasira cone and recent eruptions at Oldoinyo Lengai Volcano, Tanzania. Lithos, 152, 40–46

Moore, K. and Wood, B.J. (1998) The transition from carbonate to silicate melts in the CaO-MgO-SiO_2-CO_2 system. Journal of Petrology **39**, 1943-1952.

Morizet, Y., Kohn, S.C., and Brooker, R.A. (2001) Annealing experiments on CO_2-bearing jadeite glass: an insight into the true temperature dependence of CO_2 speciation in silicate melts. Mineralogical Magazine, 65, 701-707.

Morizet, Y., Brooker, R.A., and Kohn, S.C. (2002) CO_2 in haplo-phonolite melt: solubility, speciation and carbonate complexation. Geochimica Cosmochimica Acta, 66, 1809–1820.

Morizet, Y., Nichols, A.R.L., Kohn, S.C., Brooker, R.A., and Dingwell, D.B. (2007) The influence of H_2O and CO_2 on the glass transition temperature: insights into the effects of volatiles on magma viscosity. European Journal of Mineralogy, 19, 657-669.

Morizet, Y., Paris, M., Gaillard, F., and Scaillet, B. (2009) Raman quantification factor calibration for CO–CO_2 gas mixture in synthetic fluid inclusions: application to oxygen fugacity calculation in magmatic systems. Chemical Geology, 264, 58–70.

Morizet, Y., Paris, M., Gaillard, F., and Scaillet, B. (2010) C-O-H fluid solubility in haplobasalt under reducing conditions: An experimental study. Chemical Geology, 279, 1-16.

Mormone, A., Piochi, M., Bellatreccia, F., De Astis, G., Moretti, R., Della Ventura, G., Cavallo, A., and Mangiacapra, A. (2011) A CO_2-rich magma source beneath the Phlegraean Volcanic District (Southern Italy): Evidence from a melt inclusion study. Chemical Geology, 287, 66-80.

Mysen, B.O., Virgo, D., and Scarfe, C.M. (1980) Relations between the anionic structure and viscosity of silicate melts – a Raman spectroscopic study. American Mineralogist, 65, 690-710.

Mysen, B.O., Virgo, D., and Seifert, F.A. (1982) The structure of silicate melts: implications for chemical and physical properties of natural magma. Reviews of Geophysics and Space Physics, 20, 353-383.

826 Mysen, B.O. and Virgo, D. (1980a) Solubility mechanisms of carbon dioxide in silicate
827 metals: a Raman spectroscopic study. American Mineralogist, 65, 885-899.

828

829 Mysen, B.O. and Virgo, D. (1980b) Solubility mechanisms of water in basalt melt at high
830 pressures and temperatures: $NaCaAlSi_2O_7$-H_2O as a model. American Mineralogist, 65,
831 1176-1184.

832

833 Mysen, B.O. and Richet, P. (2005) Silicate glasses and melts: Properties and structure. 560
834 pp.

835

836 Mysen, B.O. (1988) Structure and properties of silicate melts. Developments in
837 Geochemistry, vol. 4. Elsevier, Amsterdam, 354 pp.

838

839 Mysen, B.O. (2007) The solution behavior of H_2O in peralkaline aluminosilicate melts at
840 high pressure with implications for properties of hydrous melts. Geochimica Cosmochimica
841 Acta, 71, 1820-1834.

842

843 Neuville, D.R. and Mysen, B.O. (1996) Role of the Al in the silicate network: in situ, high
844 temperature study of glasses and melts on the join SiO_2-$NaAlO_2$. Geochimica Cosmochimica
845 Acta, 60, 1727-1737.

846

Neuville, D.R., Cormier, L., and Massiot, D. (2004) Al environment in tectosilicate and peraluminous glasses: a ^{27}Al MQMAS NMR, Raman, and XANES investigation. Geochimica Cosmochimica Acta, 68, 5071–5079.

Oppenheimer, C., Moretti, R., Kyle, P.R., Eschenbacher, A., Lowenstern, J.B., Hervig, R.L., and Dunbar, N.W. (2011) Mantle to surface degassing of alkalic magmas at Erebus volcano, Antartica. Earth Planetary Science Letters, 306, 261-271.

Pan, V., Holloway, J.R., and Hervig, R.L. (1991) The pressure and temperature dependence of carbon dioxide solubility in tholeiitic basalt melts. Geochimica Cosmochimica Acta, 55, 1587–1595.

Papale, P. and Polacci, M. (1999) Role of carbon dioxide in the dynamics of magma ascent in explosive eruptions. Bulletin of Volcanology, 60, 583-594.

Pasquarello, A. and Car, R. (1998) Identification of Raman defect lines as signatures of ring structures in vitreous silica. Physical Review Letters, 80, 5145–5147.

Pyle, J.M. and Haggerty, S.E. (1994) Silicate-carbonate liquid immiscibility in upper-mantle eclogites: Implications for natrosilicic and carbonatitic conjugate melts. Geochimica et Cosmochimica Acta, 58**,** 2997-3011.

Rai, C.S., Sharma, S.K., Muenow, D.W., Matson, D.W., and Byers, C.D. (1983) Temperature dependence of CO_2 solubility in high pressure quenched glass of diopside composition. Geochimica Cosmochimica Acta, 47, 953–958.

Rividi, N., Van Zuilen, M., Philippot, P., Ménez, B., Godard, G., and Poidatz, E. (2010) Calibration of carbonate composition using Micro-Raman analysis: Application to planetary surface exploration. Astrobiology, 10, 293-309.

Robinet, L., Bouquillon, A., and Hartwig, J. (2008) Correlations between Raman parameters and elemental composition in lead and lead alkali silicate glasses. Journal of Raman Spectroscopy, 39, 618–626.

Rossano, S. and Mysen, B.O. (2013) Raman spectroscopy of silicate glasses and melts in geological system. In: Dubessy J., Caumon M.C., Rull F. (eds) Raman spectroscopy applied to Earth Sciences and Cultural Heritage (EMU notes in Mineralogy) Mineralogical Society of America, 12, pp 321-366.

Rutt, H.N. and Nicola, J.H. (1974) Raman spectra of carbonates of calcite structure. Journal of Physics C Solid State Physics, 7, 4522-4528.

889 Seifert, F.A., Mysen, B.O., and Virgo, D. (1982) Three-dimensional network structure in the
890 systems SiO_2-$NaAlO_2$, SiO_2-$CaAl_2O_4$ and SiO_2-$MgAl_2O_4$. American Mineralogist, 67, 696-
891 711.

892

893 Sharma, S.K., Mammone, J.F., and Nicol, M.F. (1981) Raman investigation of ring
894 configurations in vitreous silica. Nature, 292, 140-141..

895

896 Shimizu, K., Shimizu, N., Komiya, T., Suzuki, K., Maruyama, S., and Tatsumi, Y. (2009)
897 CO_2-rich komatiitic melt inclusions in Cr-spinels within beach sand from Gorgona Island,
898 Colombia. Earth Planetary Science Letters, 288, 33-43.

899

900 Spickenbom, K. Sierralra, M. and Nowak, M. (2010) Carbon dioxide and argon diffusion in
901 silicate melts: Insights into the CO_2 speciation in magmas. Geochimica Cosmochimica Acta,
902 74, 6541-6564.

903

904 Stolper, E.M. and Holloway, J.R. (1988) Experimental determination of the solubility of
905 carbon dioxide in molten basalt at low-pressure. Earth Planetary Science Letters, 87, 397–
906 408.

907

908 Symonds, R.B., Rose, W.I., Bluth, G.J.S., and Gerlach, T.M. (1994) Volcanic-gas studies:
909 Methods, Results and Applications. In: Carroll M.R., Holloway J.R. (eds) Volatiles in

magmas. (Reviews in mineralogy) Mineralogical Society of America, Washington, DC, 30, pp 1-66.

Tamic, N., Behrens, H., and Holtz, F. (2001) The solubility of H_2O and CO_2 in rhyolitic melts in equilibrium with a mixed CO_2–H_2O fluid phase. Chemical Geology, 174, 333–347.

Tarcea, N. and Popp, J. (2013) Raman data analysis. In: Dubessy J., Caumon M.C., Rull F. (eds) Raman spectroscopy applied to Earth Sciences and Cultural Heritage (EMU notes in Mineralogy) Mineralogical Society of America, 12, pp 193-226.

Thibault, Y. and Holloway, J.R. (1994) Solubility of CO_2 in a Ca-rich leucitite: Effects of pressure, temperature, and oxygen fugacity. Contribution to Mineralogy and Petrology, 116, 216–224.

Thomas, R. (2000) Determination of water contents of granite melt inclusions by confocal laser Raman microprobe spectroscopy. American Mineralogist, 85, 868–872.

Thomas, R., Metrich, N., Scaillet, B., Kamenetsky, V., and Davidson, P. (2008) Determination of water in Fe-rich basalt glasses with confocal micro-Raman spectroscopy. Zeitschrift für Geologische Wissenschaften, 36, 31–37.

931 Vetere, F., Botcharnikov, R.E., Holtz, F., Behrens, H., and De Rosa, R. (2011) Solubility of
932 H_2O and CO_2 in shoshonitic melts at 1250°C and pressures from 50 to 400 MPa: Implications
933 for Campi Flegrei magmatic systems. Journal of Volcanology and Geothermal Research, 202,
934 251-261.

935

936 Wu, Y.Q., Jiang, G.C., You, J.L., Hou, H.Y., Chen, H., and Xu, K.D. (2004) Theoretical
937 study of the local structure and Raman spectra of CaO-SiO_2 binary melts. Journal of
938 Chemical Physics, 121, 7883-7895.

939

940 Zajacz, Z., Halter, W., Malfait, W.J., Muntener, O., Bodnar, R.J., Bahcmann, O., Webster,
941 J.D., Ulmer, P., Mandeville, C.W., Hirschmann, M.M., and Morizet, Y. (2005) A
942 composition independent quantitative determination of the water content in silicate glasses
943 and silicate melt inclusions by confocal Raman-spectroscopy. Contribution to Mineralogy
944 and Petrology, 150, 631–642.

945

946 Figure caption

947 Figure 1. Typical Raman spectra. The spectra illustrate the silicate melt bands in the
948 HF (800-1200 cm^{-1}) and LF (200-600 cm^{-1}) regions as well as the typical Raman band for ν_1
949 CO_3 peak at ~1070 cm^{-1}. (A) Raman spectra obtained for YP phonolite samples: YPF,
950 volatile-free; YP39, 0.75 wt.% CO_2; YP11, 1.41 wt.% CO_2; and YP22, 1.99 wt.% CO_2. (B)
951 Raman spectra obtained for other selected glass compositions. RB117 shows a ν_1 CO_3^{2-}
952 which is composed of two peaks suggesting two different CO_3^{2-} environments. (C) Raman
953 spectra showing the characteristics of contamination, by Epoxy resin and Olympus x50
954 objective. RB107 is used as an example to show the spectra before and after subtraction of
955 contamination.

956

957 Figure 2. Examples of baseline curves fitted to the Raman spectra. In (A), (C) and
958 (D), the baseline is constrained by three anchor points at 250, 800 and 1250 cm^{-1}. In (B), the
959 second anchor is located between 600 and 700 cm^{-1}. The fitted baseline is a third order
960 polynomial function.

961

962 Figure 3. Raman spectra simulated with four individual Gaussian peaks for the
963 aluminosilicate Q-species and one Gaussian peak for the ν_1 vibration of CO_3^{2-}. The CO_2-free
964 haplo-phonolite YPF was first simulated with fours Gaussian peaks in A. Typical peak
965 positions are 921, 997, 1070 and 1132 cm^{-1}. For CO_2-bearing equivalents (YP12, 11 and 22),
966 the Raman spectra (B to D) were simulated with an additional peak for ν_1 CO_3^{2-} along with
967 Q-species peak position obtained for YPF sample. The ν_1 CO_3^{2-} peak position changes from
968 1082 to 1084 cm^{-1} for the illustrated samples.

969

970 Figure 4. Simulation of the Raman spectra for other selected glass compositions with
971 various CO_2 contents to illustrate the variation in HF envelope shape as well as the ν_1 CO_3^{2-}
972 peak intensity. The simulations show examples requiring different numbers of Q-species
973 Gaussian peaks (3 to 6) to fit the spectra as well a one or two (in F) peaks for ν_1 CO_3^{2-}. The
974 peak positions representing the different Q-species change as a function of glass composition.
975 For instance, in polymerized glasses (NBO/T close to 0), a peak at 1130-1150 cm^{-1} is
976 required (see B, D and E) whereas for the depolymerised glass, this peak is not required, but
977 instead a peak at 860-880 cm^{-1} is necessary (see C).

978

979 Figure 5. The fitted ratio of CO_3/HF as a function of the wt.% CO_2 measured by
980 LECO and FTIR. The entire CO_2 dataset is plotted in A, whilst the lower concentration range
981 from 0 to 1 wt.% CO_2 is shown in more detail in B. The error bar on each data point
982 represents the propagated error for the CO_3/HF ratios assuming an error of 5% on the
983 determined peaks area from the simulation. The different symbols correspond to three subsets
984 of the database: the YP phonolite, All other compositions with one ν_1 CO_3^{2-} peak and
985 Compositions with two ν_1 CO_3^{2-} peaks. The equation obtained from the linear regression and
986 the fit (R^2) is also reported.

987

988 Figure 6. Shifts in the carbonate ν_1 CO_3^{2-} peak position as a function of calculated
989 melt density for haplo-phonolite samples of Morizet et al. (2002). Densities were calculated
990 at the experimental equilibration conditions using the model of Lange and Carmichael
991 (1990). An error of ±0.5 cm^{-1} is applied to the carbonate ν_1 CO_3^{2-} peak position.

992

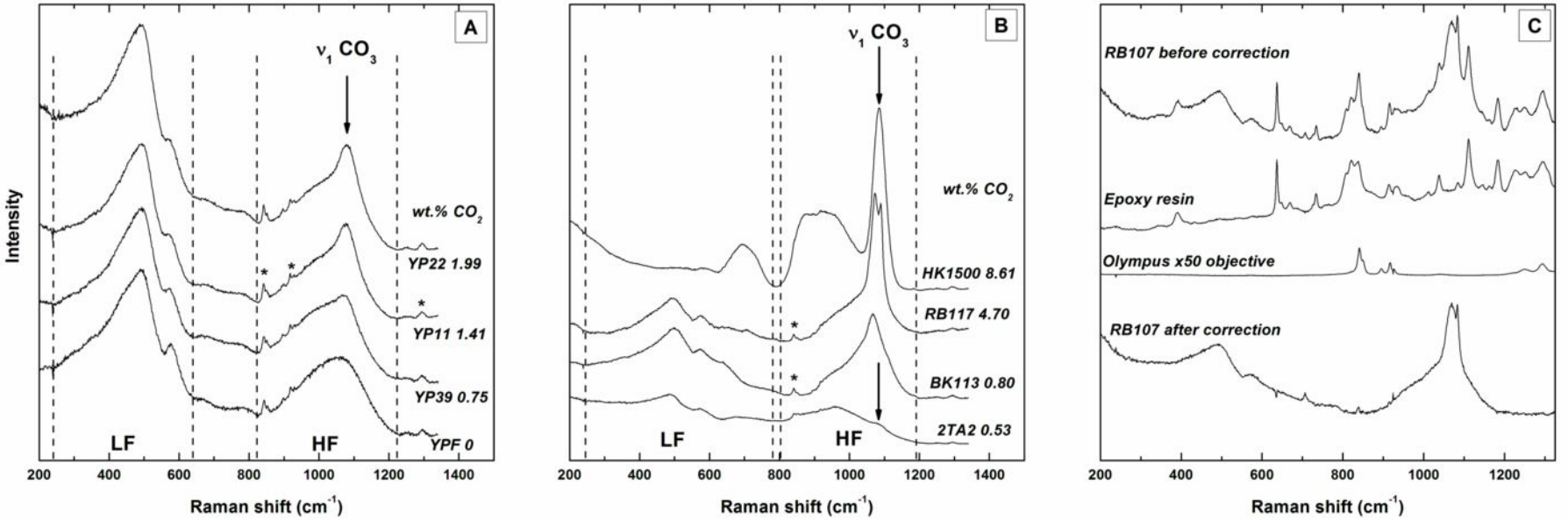
A
ν_1 CO_3
wt.% CO_2
YP22 1.99
YP11 1.41
YP39 0.75
YPF 0
LF
HF
Intensity
Raman shift (cm^{-1})
B
ν_1 CO_3
wt.% CO_2
HK1500 8.61
RB117 4.70
BK113 0.80
2TA2 0.53
LF
HF
Raman shift (cm^{-1})
C
RB107 before correction
Epoxy resin
Olympus x50 objective
RB107 after correction
Raman shift (cm^{-1})

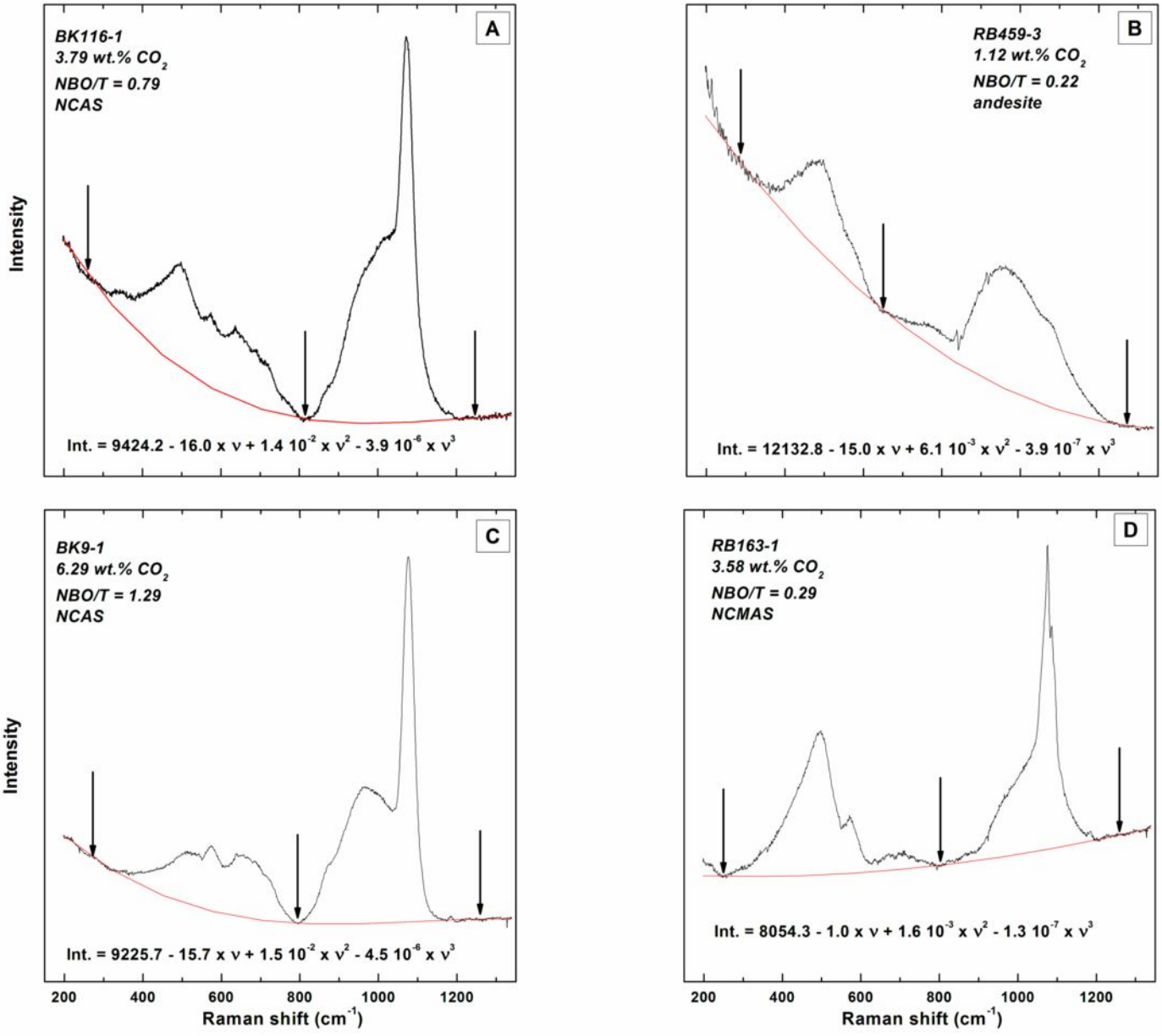
A
BK116-1
3.79 wt.% CO2
NBO/T = 0.79
NCAS
Int. = 9424.2 - 16.0 x ν + 1.4 10-2 x ν2 - 3.9 10-6 x ν3
B
RB459-3
1.12 wt.% CO2
NBO/T = 0.22
andesite
Int. = 12132.8 - 15.0 x ν + 6.1 10-3 x ν2 - 3.9 10-7 x ν3
C
BK9-1
6.29 wt.% CO2
NBO/T = 1.29
NCAS
Int. = 9225.7 - 15.7 x ν + 1.5 10-2 x ν2 - 4.5 10-6 x ν3
D
RB163-1
3.58 wt.% CO2
NBO/T = 0.29
NCMAS
Int. = 8054.3 - 1.0 x ν + 1.6 10-3 x ν2 - 1.3 10-7 x ν3
Intensity
Intensity
200 400 600 800 1000 1200
Raman shift (cm-1)
200 400 600 800 1000 1200
Raman shift (cm-1)

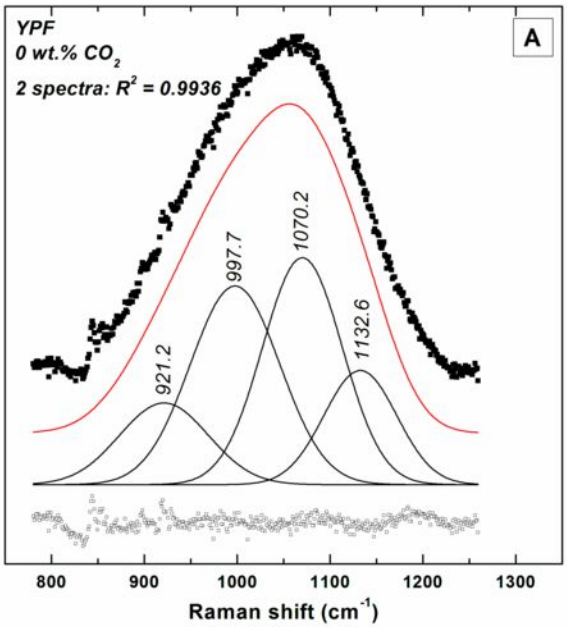
YPF
0 wt.% CO_2
2 spectra: R^2 = 0.9936
A
921.2
997.7
1070.2
1132.6
800
900
1000
1100
1200
1300
Raman shift (cm^{-1})

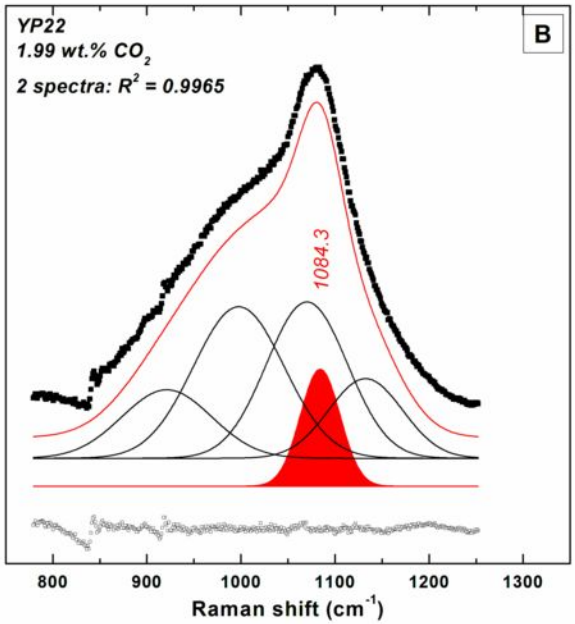
YP22
1.99 wt.% CO_2
2 spectra: R^2 = 0.9965
B
1084.3
800
900
1000
1100
1200
1300
Raman shift (cm^{-1})

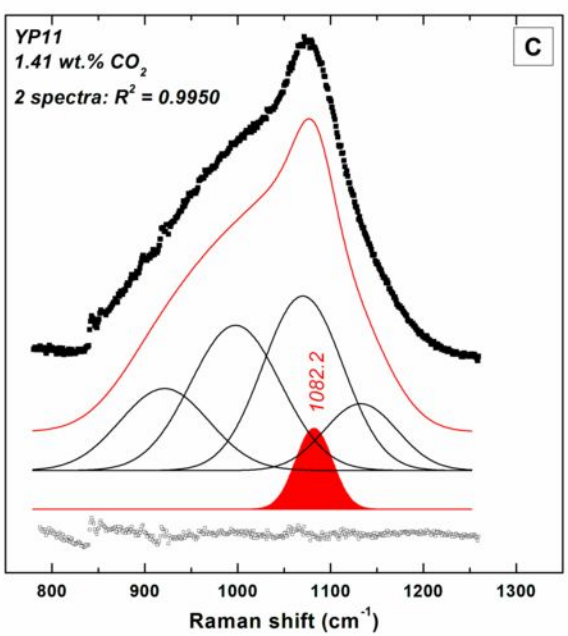
YP11
1.41 wt.% CO_2
2 spectra: R^2 = 0.9950
C
1082.2
800
900
1000
1100
1200
1300
Raman shift (cm^{-1})

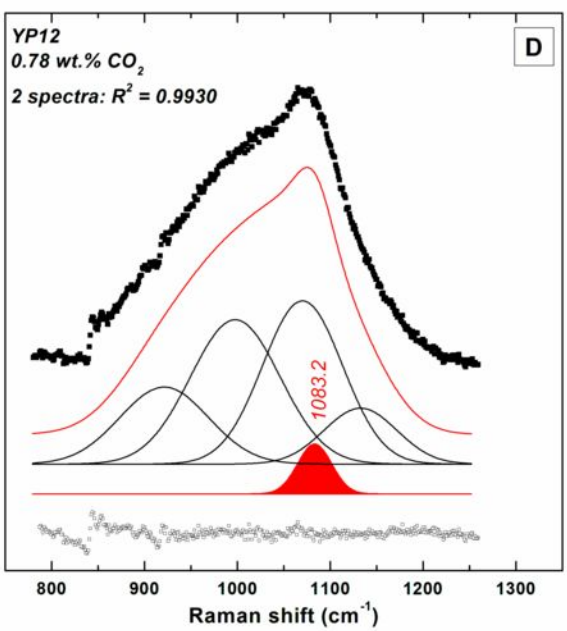
YP12
0.78 wt.% CO_2
2 spectra: R^2 = 0.9930
D
1083.2
800
900
1000
1100
1200
1300
Raman shift (cm^{-1})

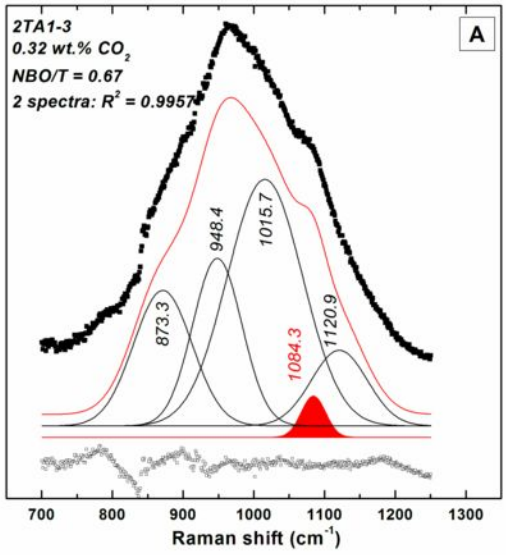
2TA1-3
0.32 wt.% CO2
NBO/T = 0.67
2 spectra: R2 = 0.9957
A
873.3
948.4
1015.7
1084.3
1120.9
700 800 900 1000 1100 1200 1300
Raman shift (cm-1)

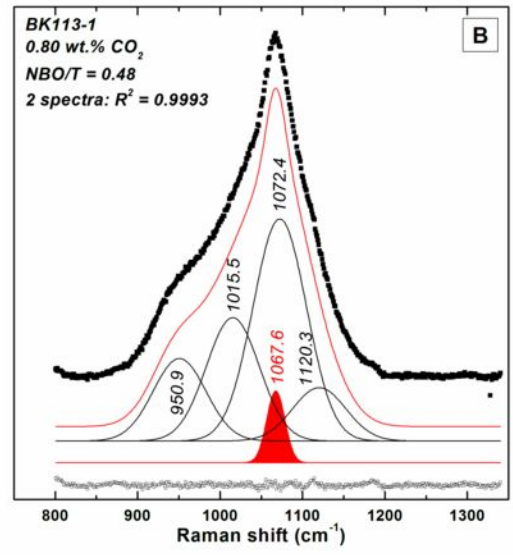
BK113-1
0.80 wt.% CO2
NBO/T = 0.48
2 spectra: R2 = 0.9993
B
950.9
1015.5
1067.6
1072.4
1120.3
800 900 1000 1100 1200 1300
Raman shift (cm-1)

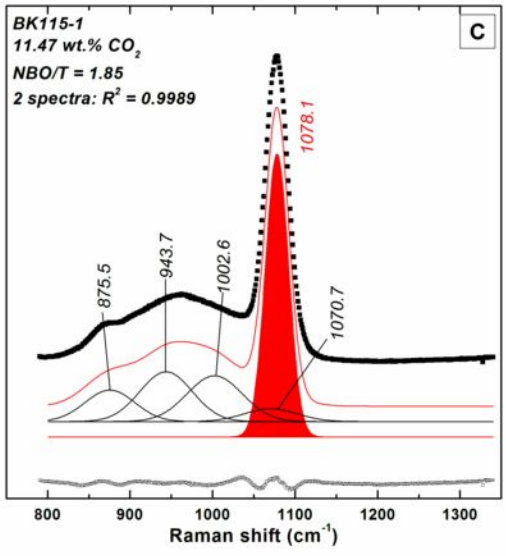
BK115-1
11.47 wt.% CO2
NBO/T = 1.85
2 spectra: R2 = 0.9989
C
875.5
943.7
1002.6
1070.7
1078.1
800 900 1000 1100 1200 1300
Raman shift (cm-1)

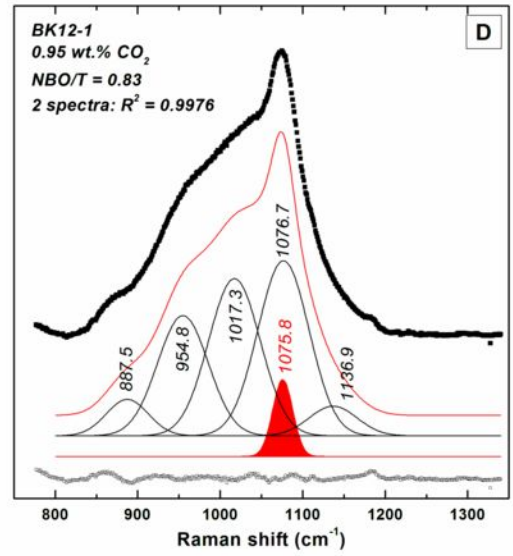
BK12-1
0.95 wt.% CO2
NBO/T = 0.83
2 spectra: R2 = 0.9976
D
887.5
954.8
1017.3
1075.8
1076.7
1136.9
800 900 1000 1100 1200 1300
Raman shift (cm-1)

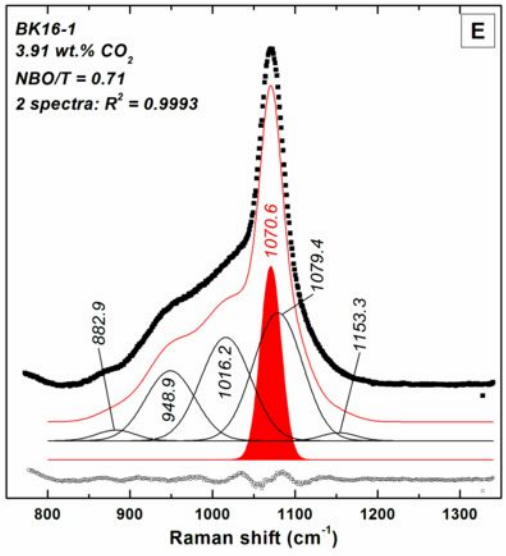
BK16-1
3.91 wt.% CO2
NBO/T = 0.71
2 spectra: R2 = 0.9993
E
882.9
948.9
1016.2
1070.6
1079.4
1153.3
800 900 1000 1100 1200 1300
Raman shift (cm-1)

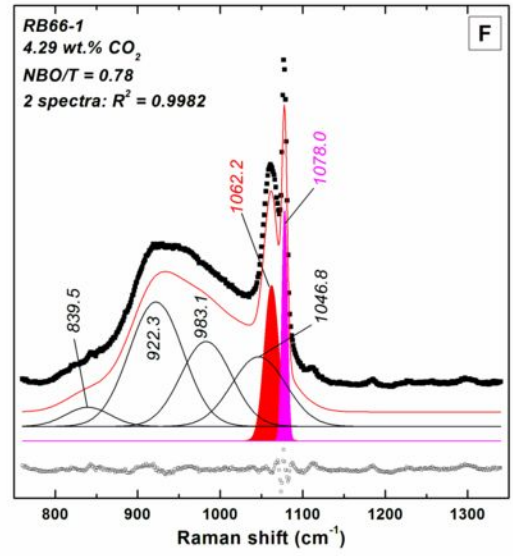
RB66-1
4.29 wt.% CO2
NBO/T = 0.78
2 spectra: R2 = 0.9982
F
839.5
922.3
983.1
1046.8
1062.2
1078.0
800 900 1000 1100 1200 1300
Raman shift (cm-1)

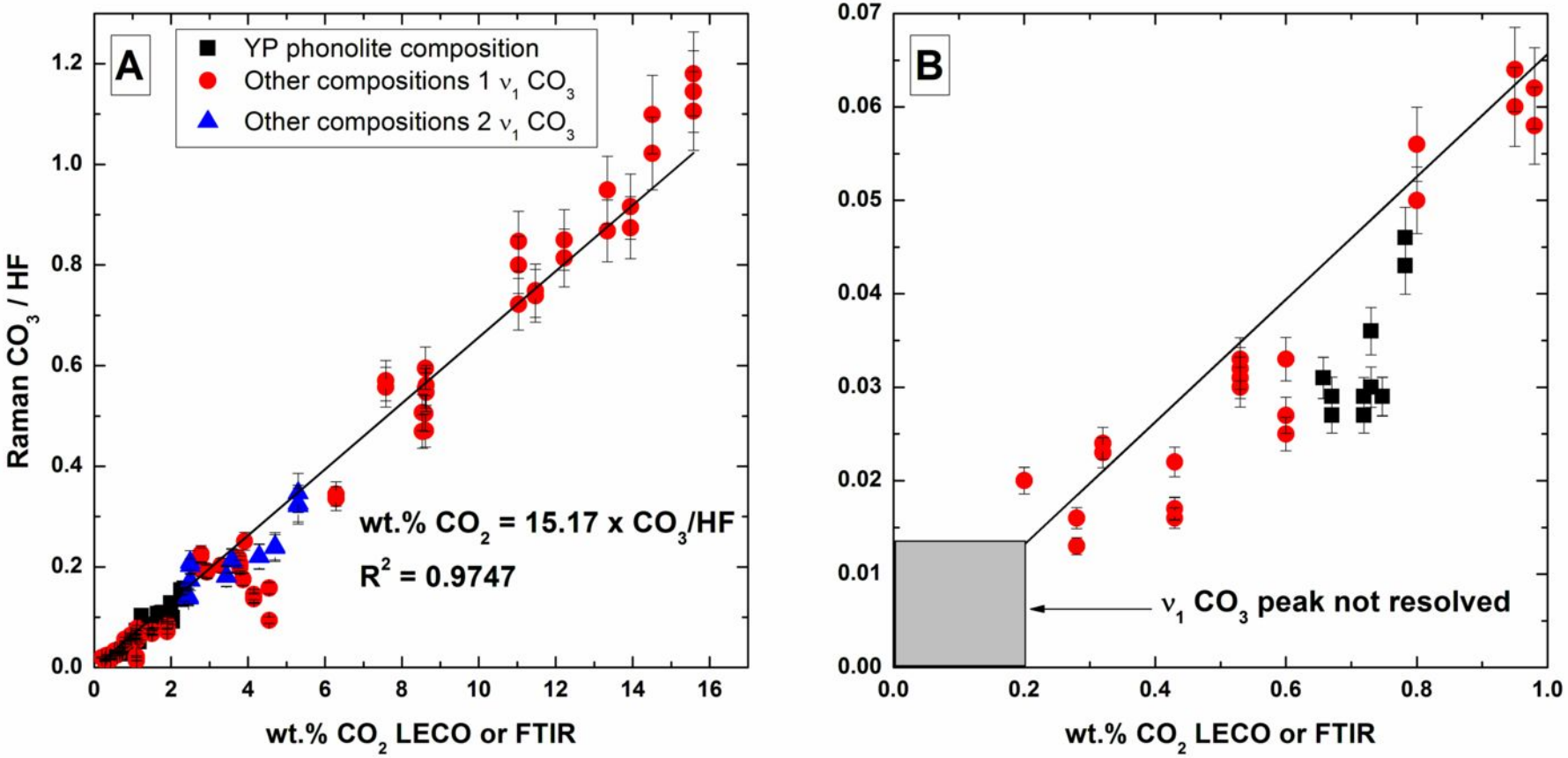
A
YP phonolite composition
Other compositions 1 ν1 CO3
Other compositions 2 ν1 CO3
wt.% CO2 = 15.17 x CO3/HF
R2 = 0.9747
Raman CO3 / HF
wt.% CO2 LECO or FTIR
B
ν1 CO3 peak not resolved
wt.% CO2 LECO or FTIR

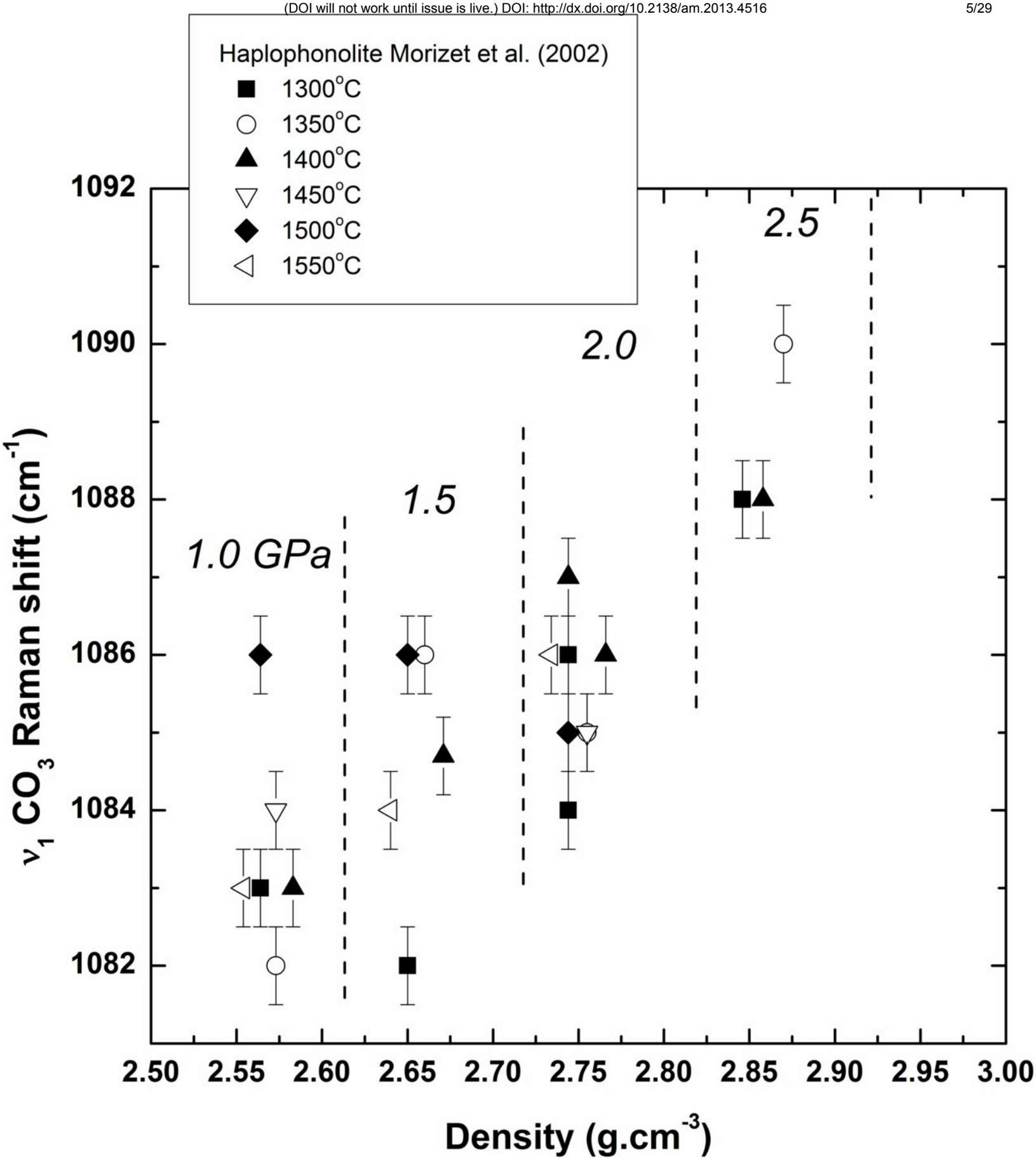
Haplophonolite Morizet et al. (2002)
1300°C
1350°C
1400°C
1450°C
1500°C
1550°C
1.0 GPa
1.5
2.0
2.5
1092
1090
1088
1086
1084
1082
ν1 CO3 Raman shift (cm-1)
2.50
2.55
2.60
2.65
2.70
2.75
2.80
2.85
2.90
2.95
3.00
Density (g.cm-3)

Table 1: Sample dataset of various glass compositions.

Sample	wt.% CO_2*	NBO/T†	Peralkalinity‡	Glass Composition§	Reference#
YPF	0	0.18	0.994	haplo-phonolite	[1]
YP34	0.66	0.18	0.994	haplo-phonolite	[1]
YP35	0.67	0.18	0.994	haplo-phonolite	[1]
YP7	0.72	0.18	0.994	haplo-phonolite	[1]
YP10	0.73	0.18	0.994	haplo-phonolite	[1]
YP39	0.75	0.18	0.994	haplo-phonolite	[1]
YP12	0.78	0.18	0.994	haplo-phonolite	[1]
YP33	1.08	0.18	0.994	haplo-phonolite	[1]
YP6	1.1	0.18	0.994	haplo-phonolite	[1]
YP9	1.17	0.18	0.994	haplo-phonolite	[1]
YP31	1.23	0.18	0.994	haplo-phonolite	[1]
YP11	1.41	0.18	0.994	haplo-phonolite	[1]
YP3	1.56	0.18	0.994	haplo-phonolite	[1]
YP30	1.65	0.18	0.994	haplo-phonolite	[1]
YP2	1.66	0.18	0.994	haplo-phonolite	[1]
YP20	1.74	0.18	0.994	haplo-phonolite	[1]
YP29	1.79	0.18	0.994	haplo-phonolite	[1]
YP28	1.91	0.18	0.994	haplo-phonolite	[1]
YP4	1.99	0.18	0.994	haplo-phonolite	[1]
YP22	1.99	0.18	0.994	haplo-phonolite	[1]
YP54	2.04	0.18	0.994	haplo-phonolite	unpublished
YP37	2.26	0.18	0.994	haplo-phonolite	unpublished
YP36	2.35	0.18	0.994	haplo-phonolite	unpublished
2TA1	0.32	0.67	0.773	trachy-andesite	[2]
2TA2	0.53	0.85	0.736	basaltic trachy-andesite	[2]
2TA3	0.98	1.15	0.731	tephrite	[2]
#4-3	0.20	0.80	0.385	alkali-basalt	[3]
#4-4	0.43	0.98	0.396	alkali-basalt	[3]
#5-5	0.60	1.08	0.415	alkali-basalt	[3]
EtnaCO22702	0.28	0.68	0.480	alkali-basalt	unpublished
RB459	1.12	0.22	0.392	andesite	[4]
RB465	1.5	0.13	0.889	phonolite	[4]
RB461	1.51	0.13	0.889	phonolite	[4]
RB108	2.45	0.34	2.029	NCAS system	[4]
RB107	2.5	0.41	2.038	NCAS system	[4]
RB99	2.78	0.39	1.457	NCAS system	[4]
RB100	2.93	0.32	1.535	NCAS system	[4]
RB102	3.3	0.44	1.292	NCAS system	[4]
RB134	3.44	0.45	1.531	NCMAS system	[4]
RB163	3.58	0.29	1.557	NCMAS system	[4]
RB159	3.75	0.22	1.288	NCMAS system	[4]
RB66	4.29	0.78	0.394	NCAS system	[4]

RB439	4.55	1.16	0.466	Mg-nephelinite	[4]
RB117	4.7	0.58	1.848	NCMAS system	[4]
RB138	5.3	0.83	2.035	NCMAS system	[4]
RB84	8.6	2.27	1.003	NCAS system	[4]
RB8	15.58	1.96	0.889	NCAS system	[4]
BK113	0.8	0.48	2.151	NCAS system	[5]
BK12	0.95	0.83	0.999	NCAS system	[5]
BK116	3.79	0.79	1.545	NCAS system	[5]
BK3	3.87	1.32	1.021	NCAS system	[5]
BK16	3.91	0.71	2.051	NCAS system	[5]
BK9	6.29	1.29	0.965	NCAS system	[5]
BK32	8.53	1.58	2.195	NCAS system	[5]
BK115	11.47	1.85	1.008	NCAS system	[5]
HK1500	8.61	2.42	0.962	haplo-kimberlite	[6]
HK1580	8.63	2.42	0.962	haplo-kimberlite	[6]
R85Ca15	12.22	2.00	0	NCAS system	[6]
RCcNa15	13.34	2.00	0.498	NCAS system	[6]
AbCcNa10	14.51	2.00	2.001	NCAS system	[6]
RB466	1.1	0.22	0.392	andesite	unpublished
BK236	1.9	0.33	0.939	phonolite	unpublished
BK237	4.15	0.58	0.979	néphélinite	unpublished
BK39	7.58	1.94	2.299	NCAS system	unpublished
BK38	11.03	2.00	2.302	NCAS system	unpublished
BK48	13.94	2.35	1.69	NCAS system	unpublished

* The reported wt.% CO_2 was determined from replicated bulk analyses in references [1], [3], [4] and [5]. The reported wt.% CO_2 in [2] is determined from micro-FTIR measurements and Beer-Lambert law.

† The NBO/T describing the average polymerisation was calculated using the definition of Mysen (1988, 1990).

‡ The peralkalinity is defined as the molar ratio $(Na_2O+K_2O)/Al_2O_3$. For a ratio above 1, the glass is peralkaline and for a ratio below 1, the glass is peraluminous.

§ The glass compositions are not represented for clarity but can be found in Supplementary material. NCAS system: Na_2O-CaO-Al_2O_3-SiO_2; NCMAS system: Na_2O-CaO-MgO-Al_2O_3-SiO_2.

[2] References: [1], Morizet et al. (2002); [2], Iacono-Marziano et al. (2012); [3], Iacono-Marziano et al. (2008); [4] Brooker et al. (2001a); [5], Brooker and Kjarsgaard (2011); [6], Brooker et al. (2011).

Table 2: Raman spectra simulation results for CO_3 and silicate glass structure and calculated CO_2 content.

Samples	Peak positions and FWHM (cm^{-1})*							CO_3/HF‡	Calculated CO2 content from linear regression
	CO_3†	Q^n pk1	Q^n pk2	Q^n pk3	Q^n pk4	Q^n pk5	Q^n pk6		
YPF-1§		1133	1070	998	921			0.000	0.000
YPF-2		78.6	85.9	96.5	95.6			0.000	0.000
YP34-1	1082							0.031 ±0.002	0.48 ±0.03
YP34-2	34.2							0.031 ±0.002	0.47 ±0.03
YP35-1	1084							0.029 ±0.002	0.44 ±0.03
YP35-2	37.5							0.027 ±0.002	0.41 ±0.03
YP7-1	1086							0.027 ±0.002	0.41 ±0.03
YP7-2	36.6							0.029 ±0.002	0.44 ±0.03
YP10-1	1083							0.036 ±0.003	0.54 ±0.04
YP10-2	38.2							0.030 ±0.002	0.46 ±0.03
YP39-1	1083							0.029 ±0.002	0.45 ±0.03
YP39-2	34.9							0.029 ±0.002	0.44 ±0.03
YP12-1	1083							0.046 ±0.003	0.69 ±0.05
YP12-2	36.8							0.043 ±0.003	0.66 ±0.05
YP33-1	1084							0.062 ±0.004	0.94 ±0.07
YP33-2	40.2							0.061 ±0.004	0.93 ±0.07
YP6-1	1086							0.069 ±0.005	1.04 ±0.07
YP6-2	40.6							0.073 ±0.005	1.10 ±0.08
YP9-1	1084.7							0.051 ±0.004	0.77 ±0.05
YP9-2	39.8							0.051 ±0.004	0.77 ±0.05
YP31-2	1086 42.4							0.103 ±0.007	1.56 ±0.11
YP11-1	1082							0.083 ±0.006	1.26 ±0.09
YP11-2	39.5							0.073 ±0.005	1.11 ±0.08
YP3-1	1085							0.083 ±0.006	1.26 ±0.09
YP3-2	41.2							0.086 ±0.006	1.30 ±0.09
YP30-1	1086							0.104 ±0.007	1.58 ±0.11
YP30-2	42.0							0.107 ±0.008	1.63 ±0.12
YP2-1	1086							0.105 ±0.007	1.59 ±0.11
YP2-2	43.3							0.103 ±0.007	1.57 ±0.11
YP20-1	1087							0.108 ±0.008	1.63 ±0.12
YP20-2	41.7							0.099 ±0.007	1.50 ±0.11
YP29-1	1085							0.103 ±0.007	1.56 ±0.11
YP29-2	41.6							0.109 ±0.008	1.66 ±0.12
YP28-1	1085							0.094 ±0.007	1.42 ±0.10
YP28-2	45.4							0.098 ±0.007	1.49 ±0.11
YP4-1	1086							0.128 ±0.009	1.94 ±0.14
YP4-2	46.3							0.123 ±0.009	1.87 ±0.13
YP22-1	1084							0.114 ±0.008	1.73 ±0.12
YP22-2	42.2							0.119 ±0.008	1.81 ±0.13
YP54-1	1090							0.099 ±0.007	1.49 ±0.11

YP54-2	44.1						0.092 ±0.007	1.40 ±0.10
YP37-1	1088						0.154 ±0.011	2.33 ±0.16
YP37-2	41.6						0.135 ±0.010	2.05 ±0.15
YP36-1	1088						0.141 ±0.010	2.14 ±0.15
YP36-2	43.1						0.157 ±0.011	2.38 ±0.17
2TA2-1[P]							0.033 ±0.002	0.50 ±0.04
2TA2-2	1084	1118		1017	953	879	0.030 ±0.002	0.45 ±0.03
2TA2-3	32.5	74.3		103.7	66.3	80.5	0.031 ±0.002	0.48 ±0.03
2TA2-4							0.032 ±0.002	0.48 ±0.03
2TA3-1	1083	1110		1012	951	877	0.062 ±0.004	0.93 ±0.07
2TA3-2	33.0	74.1		102.3	65.1	78.2	0.058 ±0.004	0.88 ±0.06
2TA1-1	1084	1121		1016	948	873	0.024 ±0.002	0.35 ±0.03
2TA1-2	34.3	79.1		106.6	69.6	82.6	0.023 ±0.002	0.37 ±0.02
#4-3-1	1080		1098	1023	956	886	0.020 ±0.001	0.31 ±0.02
#4-3-2	34.7		78.5	77.4	70.7	69.6	0.020 ±0.001	0.30 ±0.02
#4-4-1							0.022 ±0.002	0.34 ±0.02
#4-4-2	1079		1071	1001	938	874	0.017 ±0.001	0.26 ±0.02
#4-4-3	31.7		92.9	91.6	77.9	71.7	0.017 ±0.001	0.25 ±0.02
#4-4-4							0.016 ±0.001	0.24 ±0.02
#5-5-1	1077		1077	1009	944	876	0.033 ±0.002	0.50 ±0.04
#5-5-2	33.9		91.6	82.9	76.3	72.0	0.027 ±0.002	0.41 ±0.03
#5-5-3							0.025 ±0.002	0.39 ±0.03
EtnaCO22702-1	1077		1089	1022	960	894	0.016 ±0.001	0.24 ±0.02
EtnaCO22702-2	30.4		68.0	69.3	68.4	67.9	0.013 ±0.001	0.19 ±0.01
RB459-1	1087	1134		1028	956	898	0.078 ±0.006	1.19 ±0.08
RB459-2	45.1	81.9		93.7	80.6	75.6	0.055 ±0.004	0.84 ±0.06
RB465-1	1081	1107	1030	962	911		0.068 ±0.005	1.04 ±0.07
RB465-2	39.2	74.5	78.3	69.9	69.5		0.068 ±0.005	1.03 ±0.07
RB461-1	1083	1114	1044	971	918		0.072 ±0.005	1.09 ±0.08
RB461-2	30.4	87.7	81.8	71.0	67.3		0.070 ±0.005	1.06 ±0.07
RB108-1	1070 / 1087	1110	1058	993	950		0.138 ±0.015	2.09 ±0.23
RB108-2	19.7 / 5.0	87.3	69.9	62.4	64.5		0.140 ±0.016	2.12 ±0.24
RB108-3							0.142 ±0.017	2.15 ±0.24
RB107-1	1070 / 1085	1174	1096	1037	963		0.209 ±0.023	3.17 ±0.35
RB107-2	22.5 / 5.3	83.6	67.5	67.5	66.8		0.173 ±0.019	2.63 ±0.29
RB107-3							0.202 ±0.014	3.06 ±0.22
RB99-1	1074	1148	1084	1031	959		0.222 ±0.016	3.37 ±0.24
RB99-2	23.8	84.0	71.4	83.0	74.3		0.226 ±0.016	3.43 ±0.24
RB99-3							0.195 ±0.014	2.96 ±0.21
RB100-1	1077	1117	1063	1002	952		0.190 ±0.013	2.89 ±0.20
RB100-2	22.5	72.2	61.0	51.0	54.2		0.192 ±0.014	2.92 ±0.21
RB102-1	1072	1111	1067	1002	941		0.203 ±0.014	3.08 ±0.22
RB102-2	22.1	54.6	66.8	72.0	70.0		0.203 ±0.014	3.08 ±0.22
RB134-1	1074 / 1088	1141	1077	1013	952		0.182 ±0.020	2.76 ±0.31
RB134-2	21.3 / 6.5	60.6	60.5	60.8	61.0		0.181 ±0.020	2.75 ±0.31
RB163-1	1074	1134	1072	1006	952		0.211 ±0.024	3.19 ±0.36
RB163-2	18.0	57.2	59.2	62.2	64.9		0.213 ±0.024	3.23 ±0.36

RB159-1	1071	1104	1062	1006	954			0.213 ±0.015	3.23 ±0.23
RB159-2	27.1	59.3	61.8	55.4	56.4			0.218 ±0.015	3.31 ±0.23
RB66-1	1062 / 1078		1047	983	922	840		0.220 ±0.025	3.34 ±0.37
RB66-2	17.3 / 6.3		65.5	61.2	65.6	53.9		0.221 ±0.025	3.35 ±0.37
RB439-1	1085			1030	961	882	759	0.158 ±0.011	2.40 ±0.17
RB439-2	26.9			66.1	73.4	74.3	140.1	0.094 ±0.007	1.43 ±0.10
RB117-1	1074 / 1091	1142	1076	1007	947			0.238 ±0.027	3.61 ±0.40
RB117-2	18.8 / 8.7	58.0	58.1	60.0	60.4			0.241 ±0.027	3.66 ±0.41
RB138-1	1075 / 1092		1082	1011	949	889		0.321 ±0.036	4.88 ±0.55
RB138-2	27.5 / 11.2		74.3	72.2	64.9	78.8		0.326 ±0.036	4.94 ±0.55
RB138-3								0.347 ±0.039	5.27 ±0.59
RB84-1	1076			1008	943	876		0.505 ±0.036	7.66 ±0.54
RB84-2	27.8			66.0	62.9	62.5		0.505 ±0.036	7.65 ±0.54
RB8-1	1079		1073	1002	943	876		1.145 ±0.081	17.37 ±1.23
RB8-2	26.2		66.1	67.0	57.9	55.4		1.180 ±0.083	17.91 ±1.27
RB8-3								1.106 ±0.078	16.78 ±1.19
BK113-1	1068	1120	1072	1007	951			0.050 ±0.004	0.77 ±0.05
BK113-2	21.8	64.5	64.8	63.2	63.9			0.056 ±0.004	0.85 ±0.06
BK12-1	1076	1137	1077	998	955	888		0.060 ±0.004	0.91 ±0.06
BK12-2	24.3	58.0	62.0	70.0	61.5	50.8		0.064 ±0.004	0.96 ±0.07
BK116-1	1075		1067	1003	943	892		0.207 ±0.015	3.14 ±0.22
BK116-2	25.5		77.1	67.0	50.1	60.5		0.199 ±0.014	3.02 ±0.21
BK3-1	1076		1070	1004	947	883		0.175 ±0.012	2.68 ±0.19
BK3-2	25.3		61.8	63.1	62.1	62.1		0.176 ±0.012	2.66 ±0.19
BK16-1	1071	1153	1079	1017	949	883		0.251 ±0.018	3.81 ±0.27
BK16-2	24.8	42.4	59.5	62.5	59.9	47.0		0.251 ±0.018	3.81 ±0.27
BK9-1	1077		1081	1014	950	885		0.336 ±0.024	5.10 ±0.36
BK9-2	26.0		53.3	72.6	62.3	66.7		0.345 ±0.024	5.23 ±0.37
BK32-1	1075	1073		1013	922	869		0.469 ±0.033	7.12 ±0.50
BK32-2	23.8	47.4		48.3	49.9	51.5		0.507 ±0.036	7.70 ±0.54
BK115-1	1078		1071	1016	944	876		0.749 ±0.053	11.36 ±0.80
BK115-2	26.3		64.4	64.3	63.5	60.2		0.739 ±0.052	11.21 ±0.79
HK1500-1	1085			1008	944	874		0.555 ±0.039	8.42 ±0.60
HK1500-2	36.2			81.9	66.1	61.8		0.595 ±0.042	9.03 ±0.64
HK1500-3								0.471 ±0.033	7.14 ±0.50
HK1580-1	1086			1022	932	865		0.547 ±0.039	8.51 ±0.59
HK1580-2	37.1			59.5	112.2	42.4		0.561 ±0.040	8.30 ±0.60
R85Ca15-1	1081		1052	989	939	876		0.850 ±0.060	12.90 ±0.91
R85Ca15-2	28.1		69.9	56.3	57.7	59.3		0.814 ±0.058	12.35 ±0.87
RCcNa15-1	1080		1072	1002	944	880		0.868 ±0.006	13.16 ±0.93
RCcNa15-2	26.2		60.5	64.1	59.3	58.7		0.949 ±0.007	14.40 ±1.02
AbCcNa10-1	1077		1073		949	878		1.099 ±0.078	16.67 ±1.18
AbCcNa10-2	25.2		62.7		61.3	58.0		1.022 ±0.072	15.51 ±1.10
RB466-3	1083		1094	1004	925	863	777	0.022 ±0.001	0.33 ±0.02
RB466-2	33.9		107.1	94.3	89.9	87.4	85.4	0.014 ±0.001	0.21 ±0.01
BK236-1	1076	1105		1016	948	879		0.082 ±0.006	1.34 ±0.09
BK236-2	31.1	75.9		60.5	71.1	77.2		0.085 ±0.006	1.29 ±0.09

BK236-3							0.072 ±0.005	1.09 ±0.08
BK237-1	1076	1079	1008	942	871		0.139 ±0.010	2.10 ±0.15
BK237-2	26.8	75.4	73.3	67.5	66.6		0.137 ±0.010	2.08 ±0.15
BK237-3							0.145 ±0.010	2.20 ±0.16
BK39-1	1076	1064	991	936	873		0.557 ±0.039	8.45 ±0.60
BK39-2	23.6	63.9	61.9	54.7	54.4		0.570 ±0.040	8.64 ±0.61
BK38-1	1075	1080	1009	942	855		0.722 ±0.051	10.96 ±0.77
BK38-2	23.7	53.9	73.6	63.5	68.7		0.847 ±0.060	12.84 ±0.91
BK38-3							0.800 ±0.057	12.14 ±0.86
BK48-1	1078	1072	989	935	873		0.874 ±0.062	13.25 ±0.94
BK48-2	24.0	54.5	78.0	50.2	57.4		0.916 ±0.065	13.90 ±0.98

* The numbers reported in those columns represent the Raman peak position and full width at half maximum (FWHM) as given by the simulation of the HF Raman spectra. For each parameter, we apply an error of ±0.5 cm^{-1} considering the fact that we have two analytical points separated by 1 cm^{-1}.

† For several samples, the CO_3 shows two distinct peaks: one large and one sharp. The peak position and FWHM of each peak is reported.

‡ The CO_3 / HF ratios are calculated from the area of the individual Gaussian peak obtained by the Raman spectra simulation. The error reported for each CO_3/HF was calculated through error propagation considering 5% of error on the derived peak areas.

§ The YPF sample is a volatile-free sample. The Raman spectra simulation was performed with only four individual Gaussian peaks for silicate glass structure.

⁋ For 2TA2, the Raman spectra were acquired at the same sample location but with four different laser power (between 75 and 200 mW) and same acquisition time (5x60 sec; see Supplementary material for the detailed acquisition conditions) to check the impact of the laser power on the CO_3 / HF areas ratios.